









Postwildfire Soil-Hydraulic Recovery and the Persistence of Debris Flow Hazards

Special Section:
Fire in the Earth System

Matthew A. Thomas¹ , Francis K. Rengers¹ , Jason W. Kean¹ , Luke A. McGuire² ,
Dennis M. Staley¹, Katherine R. Barnhart¹ , and Brian A. Ebel³ 

¹U.S. Geological Survey, Geologic Hazards Science Center, Golden, CO, USA, ²Department of Geosciences, University of Arizona, Tucson, AZ, USA, ³U.S. Geological Survey, Water Mission Area, Water Cycle Branch, Denver, CO, USA

Key Points:

- Developed methodology to identify time-variable thresholds for postwildfire debris flows with hydrologic and slope stability modeling
- Resultant thresholds are consistent with postwildfire debris flow observations and existing empirical thresholds in southern California
- Simulation-based framework is a tractable approach to develop warning criteria for debris flow hazard in the years following wildfire

Correspondence to:

M. A. Thomas,
matthewthomas@usgs.gov

Citation:

Thomas, M. A., Rengers, F. K., Kean, J. W., McGuire, L. A., Staley, D. M., Barnhart, K. R., & Ebel, B. A. (2021). Postwildfire soil-hydraulic recovery and the persistence of debris flow hazards. *Journal of Geophysical Research: Earth Surface*, 126, e2021JF006091. <https://doi.org/10.1029/2021JF006091>

Received 25 JAN 2021

Accepted 28 APR 2021

Abstract Deadly and destructive debris flows often follow wildfire, but understanding of changes in the hazard potential with time since fire is poor. We develop a simulation-based framework to quantify changes in the hydrologic triggering conditions for debris flows as postwildfire infiltration properties evolve through time. Our approach produces time-varying rainfall intensity-duration thresholds for runoff- and infiltration-generated debris flows with physics-based hydrologic simulations that are parameterized with widely available hydroclimatic, vegetation reflectance, and soil texture data. When we apply our thresholding protocol to a test case in the San Gabriel Mountains (California, USA), the results are consistent with existing regional empirical thresholds and rainstorms that caused runoff- and infiltration-generated debris flows soon after and three years following a wildfire, respectively. We find that the hydrologic triggering mechanisms for the two observed debris flow types are coupled with the effects of fire on the soil saturated hydraulic conductivity. Specifically, the rainfall intensity needed to generate debris flows via runoff increases with time following wildfire while the rainfall duration needed to produce debris flows via subsurface pore-water pressures decreases. We also find that variations in soil moisture, rainfall climatology, median grain size, and root reinforcement could impact the median annual probability of postwildfire debris flows. We conclude that a simulation-based method for calculating rainfall thresholds is a tractable approach to improve situational awareness of debris flow hazard in the years following wildfire. Further development of our framework will be important to quantify postwildfire hazard levels in variable climates, vegetation types, and fire regimes.

Plain Language Summary Wildfire can radically change a mountainous landscape such that even a modest rainstorm is capable of producing deadly and destructive flash flooding and debris flows. While we have tools to understand the likelihood of debris flows immediately following a fire, we lack the tools to assess debris flow hazard with time as the burned landscape recovers. We develop an approach to calculate the time-variable criteria for the initiation of postwildfire debris flows with a simulation framework that is computationally efficient and makes use of widely available input data. Our protocol produces warning criteria that are consistent with observations of debris flows immediately after and three years following a wildfire that occurred in southern California. We find that the effect of fire on the infiltration of water into soil can markedly influence the triggering conditions for debris flows. As wildfire activity extends into areas for which debris flow susceptibility is an open question, our work indicates that a simulation-based approach that can account for the time-variable effects of fire on the surface hydrology could be an effective tool to better inform the emergency management community.

1. Introduction

Wildfire is an environmental disturbance that can radically alter the vegetation cover and soil properties in watersheds. Depending on the burn severity, a fire can consume the rainfall-intercepting canopy and leaf litter and decrease the infiltration capacity of the soil (Moody et al., 2013; Santi & Rengers, 2020; Shakesby & Doerr, 2006). The hillslope hydrologic response associated with these changes is well known to include enhanced runoff and sediment transport during rainstorms, which can promote the initiation of runoff-generated debris flows (Cannon, 2001; Gabet & Bookter, 2008; Kean et al., 2011; Nyman et al., 2011). Runoff-generated debris flows present a substantial hazard for people and infrastructure downstream of burn scars (e.g., Kean, Staley, et al., 2019) and may play an important role in the long-term denudation of mountainous landscapes (e.g., Meyer et al., 2001). Hillslope erosion and rilling fuel the initiation of

© 2021. The Authors. Journal of Geophysical Research: Earth Surface published by Wiley Periodicals LLC on behalf of American Geophysical Union. This article has been contributed to by US Government employees and their work is in the public domain in the USA. This is an open access article under the terms of the Creative Commons Attribution-NonCommercial-NoDerivs License, which permits use and distribution in any medium, provided the original work is properly cited, the use is non-commercial and no modifications or adaptations are made.

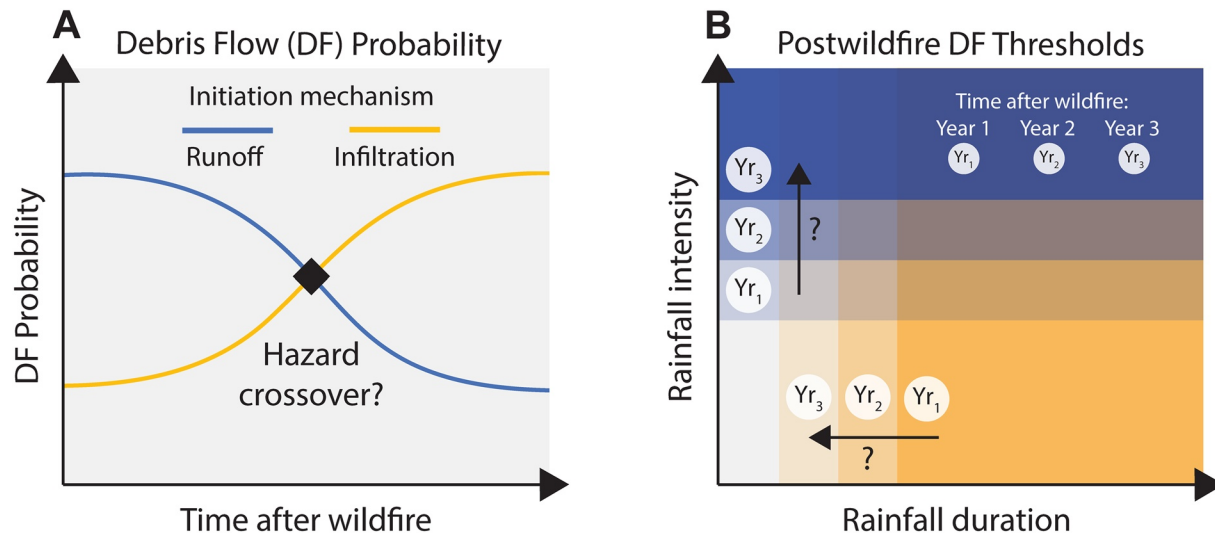


Figure 1. (a) Conceptual model for a crossover in runoff- versus infiltration-generated debris flow (DF) potential following wildfire in steep terrain. (b) Illustration of non-stationary postwildfire rainfall intensity-duration DF thresholds due to changes to infiltration properties over multi-annual timescales. Blue and orange shading corresponds to thresholds for runoff- and infiltration-generated debris flows, respectively. Higher rainfall intensities and lower rainfall durations are, respectively, needed to initiate runoff- and infiltration-generated debris flows with time after wildfire.

debris flows in soil-mantled landscapes, whereas postwildfire dry raveling is thought to be a more important mechanism in bedrock-dominated landscapes (Palucis et al., 2021). Although debris flows in the immediate aftermath of fire are commonly generated by runoff, when the landscape is particularly vulnerable to infiltration-excess overland flow (e.g., Moody & Ebel, 2014), postwildfire debris flows do not form exclusively through this mechanism (Parise & Cannon, 2012). Infiltration in response to rainfall can lead to excessive subsurface pore-water pressures that produce shallow landslides (defined as a source area length to depth ratio >10 ; Casadei et al., 2003) capable of mobilizing into debris flows (Iverson, 2000), which we refer to as infiltration-generated debris flows. In the Transverse Ranges of southern California, shallow landsliding in unburned watersheds may be responsible for roughly 50% of all hillslope erosion (Lavé & Burbank, 2004), which highlights the need to understand how their occurrence may be impacted by disturbances such as wildfire (e.g., Rengers et al., 2020). Although uncertainty in attributing above-average shallow landslide hazard potential in response to postwildfire effects is considerable (Parise & Cannon, 2012), widespread landslide activity in response to rainstorms has been observed on steep, unburned slopes in areas of southern California that routinely burn (Campbell, 1974, 1975; Rice & Foggin, 1971). These observations suggest that infiltration may be the dominant debris-flow triggering mechanism for unburned conditions and that a shift from runoff- to infiltration-generated debris flows occurs during postwildfire recovery (Figure 1a), as has been proposed for other regions in the western United States (e.g., Meyer et al., 2001; Wondzell & King, 2003).

Rainfall thresholds, which define the range of rainfall intensities and corresponding rainfall durations above which debris flows are more likely to occur, have been applied throughout the world for unburned conditions (e.g., Bell & Maud, 2000; Caine, 1980; Guzzetti et al., 2007; Hong et al., 2005; Larsen & Simon, 1993; Wilson & Jayko, 1997) and were first used for postwildfire settings in the United States more than a decade ago (Cannon, Gartner, et al., 2008; USGS, 2005). They have historically been the quantitative backbone of warning systems for debris flow initiation (Baum & Godt, 2010) and are typically based on empirical models, grounded in a power-law or polynomial functional form, that are calibrated against past debris flow events. Empirical postwildfire rainfall thresholds have seen further improvement with the use of objective calibration techniques (Staley et al., 2013), but consistent records of debris flows that distinguish between runoff- and infiltration-generated debris flows for several years after a fire are virtually nonexistent (e.g., Santi & MacAulay, 2021). The applicability of empirical postwildfire rainfall thresholds beyond the first year following fire or across regional gradients in climate, land use, and geology is challenging because how

factors such as the recovery of near-surface hillslope hydrologic functioning influence debris flow thresholds as watersheds recover from fire is not well understood (e.g., Mirus et al., 2019; Figure 1b).

Insight into the relative likelihood of postwildfire debris flows as watersheds recover would further improve our ability to predict and mitigate debris flow hazards. Computing the probability of a debris flow-producing rainstorm within the window of disturbance following fire, however, requires temporally varying estimates of the probability of producing debris flows through both runoff and infiltration generation mechanisms. Therefore, a quantitative framework to evaluate how soil-hydraulic recovery processes can influence hillslope hydrology and stability is needed to better understand the persistence of debris flow hazards after fire. In light of this knowledge gap, our objective is to develop an approach to evaluate postwildfire hillslope hydrologic response and debris flow hazard potential for runoff- and infiltration-generated debris flows as infiltration properties change. We use a combination of decadal, multi-annual, and event-based simulations to produce rainfall intensity-duration thresholds for both failure modes in the years after a wildfire. The scope of our contribution is to develop this framework and to apply it to a test case in southern California. We then discuss how our simulation-based approach could be used to elucidate the contributions of soil moisture, rainfall climatology, grain size, and root reinforcement on the probability of postwildfire debris flows. The application of our framework serves as an initial evaluation of, and an important first step toward, a quantitative method for the assessment of debris flow hazard that reflects hydrologic changes as steep watersheds recover from fire.

2. Framework Development

2.1. Simulation Timeline

At the core of our debris flow threshold framework are physics-based simulations of vertical infiltration through the unsaturated zone for climatological (decadal), postwildfire recovery (years), and event-based (≤ 24 h) timescales (Figures 2a and 2b). The simulated output for each timescale serves as an initial condition for the next. Rainfall, air temperature, and vegetation index information inform the surface boundary condition for the climatological simulation. The postwildfire recovery simulation is also forced with atmospheric and vegetation index timeseries, but the saturated hydraulic conductivity of the uppermost soil can change as a function of time to reflect fire-induced alterations to infiltration (Figures 2b and 2c). We relate changes in the saturated hydraulic conductivity to vegetation regrowth captured by remotely sensed observations of the postwildfire leaf area index (LAI), which is defined as the one-sided green leaf area per unit ground surface area (Watson, 1947). At annual intervals along the recovery timeline, we simulate an ensemble of wide-ranging rainfall intensity-duration characteristics. For each rainfall case, we track runoff at the surface and pore-water pressure at the soil-bedrock interface (i.e., the starred locations in Figures 2b and 2d) to quantify changes in failure criteria and produce simulation-based thresholds for runoff- and infiltration-generated debris flows throughout the postwildfire soil-hydraulic recovery timeline.

2.2. Numerical Flow Model and Simulation Domain

We use the HYDRUS-1D (Šimůnek et al., 2009) model to solve the Richards (1931) Equation:

$$\frac{\partial \theta}{\partial t} = \frac{\partial}{\partial z} \left[K(\psi) \left(\frac{\partial \psi}{\partial z} + 1 \right) \right] - s \quad (1)$$

where θ is the soil-water content (dimensionless), t is the time (T, time), z is the vertical spatial coordinate (L, length), K is the hydraulic conductivity (LT^{-1}), ψ is the pressure head (L), and s is a sink term associated with root-water uptake for the multi-annual simulations (T^{-1}). The finite-element domain for all three simulation types (i.e., climatological, recovery, and event based) is 10 m in height and discretized at 1 cm levels, with a water flux and pressure-dependent drain serving as the upper and lower boundary condition, respectively (Figure 2b). The climatological simulations consist of a two-layer system of shallow soil overlying weathered bedrock. The recovery and event-based simulations also include a 5 cm surficial layer representing the fire-affected soil (Figure 2b) where the saturated hydraulic conductivity varies as a function of time. We selected this fire-affected soil depth because soil temperatures are rarely $>150^\circ\text{C}$ for depths >5 cm

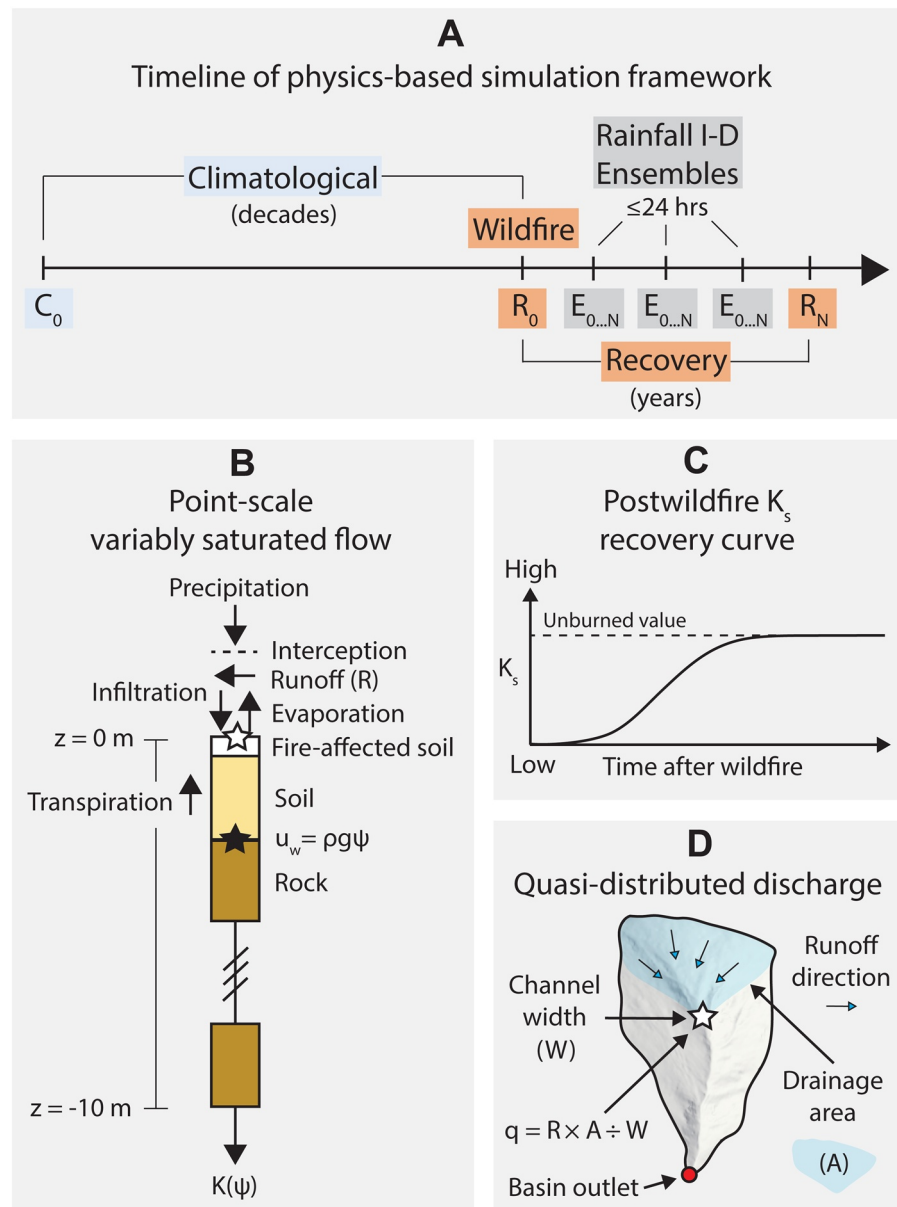


Figure 2. (a) Timeline of our simulation framework. The decadal-scale climatological phase provides an initial condition for the multi-annual recovery phase wherein we simulate the time-variable effects of wildfire on surface and near-surface hydrologic response. The recovery phase provides initial conditions for the rainfall intensity-duration frequency (ID) ensembles (i.e., a suite of high-intensity, short duration through low-intensity, long duration events) for which we track discharge (q) and subsurface pore-water pressure (u_w) during soil-hydraulic recovery. (b) Schematic of the domain that we use to simulate variably saturated flow throughout the climatological, recovery, and event-based timelines. The white and black star, respectively, indicate the locations for which we track and to evaluate runoff- and infiltration-generated debris-flow potential. (c) Example of the logistic function that we use to define fire-affected soil saturated hydraulic conductivity (K_s) as a function of time. (d) Illustration of how we scale the point-scale estimate of the runoff rate (R), drainage area (A), and channel width (W) to provide an estimate of q to evaluate runoff-generated debris flow-potential for small upland basins.

during a fire (DeBano, 2000) or $>100^{\circ}\text{C}$ for depths >10 cm (Rengers et al., 2017) and the greatest depth to unaffected soil is typically ≤ 6 cm (Moody & Ebel, 2014; Nyman et al., 2013).

2.3. Surface Fluxes

The upper boundary condition is a time-variable flux that incorporates the effects of interception, evaporation, and transpiration (Figure 2b), which are calculated for both the climatological and recovery simulation types with daily rainfall, air temperature, and vegetation index data from January 1, 1989 to a fire start date and from a fire end date to January 1, 2020, respectively. We estimate daily interception (i) (LT^{-1}) in these simulations following the von Hoyningen-Hüne (1983) approach:

$$i = c\text{LAI} \left(1 - \left(\frac{1}{1 + \frac{p\text{SCF}}{c\text{LAI}}} \right) \right) \quad (2)$$

where c is a coefficient ($c = 0.25$; Šimůnek et al., 2009), LAI is (dimensionless) interpolated from the National Aeronautics and Space Administration (NASA) Moderate Resolution Imaging Spectroradiometer (MODIS) global 500 m 8 d LAI data set (NASA 2020b) (dimensionless), p is the precipitation rate (LT^{-1}) (PRISM Climate Group, 2020), and SCF is the soil cover fraction (dimensionless). We calculate the daily SCF, which refers to the proportion of soil covered by vegetation (Šimůnek et al., 2009), for the multi-annual simulations by:

$$\text{SCF} = 1 - e^{-k\text{LAI}} \quad (3)$$

where k is the radiation extinction coefficient ($k = 0.463$; Šimůnek et al., 2009). We estimate daily potential evapotranspiration (ET_0) (LT^{-1}) for the multi-annual simulations with the Hargreaves (1994) formulation:

$$ET_0 = c_1 R_a (T_{\text{avg}} + c_2) \sqrt{(T_{\text{max}} - T_{\text{min}})} \quad (4)$$

where c_1 and c_2 are empirical constants ($c_1 = 0.0023$ and $c_2 = 17.8$; Hargreaves, 1994), R_a is the solar radiation based on the site latitude and time of the year (LT^{-1}), T_{avg} is the mean air temperature (τ , temperature), T_{max} is the maximum air temperature (τ), and T_{min} is the minimum air temperature (τ). We input the component contributions of potential evaporation (E_0) (LT^{-1}) and potential transpiration (T_0) (LT^{-1}), given by Šimůnek et al. (2009) as:

$$E_0 = ET_0(1 - \text{SCF}) \quad (5)$$

$$T_0 = ET_0\text{SCF} \quad (6)$$

HYDRUS-1D estimates actual evapotranspiration with the E_0 , T_0 , ψ solution, and a water uptake stress response function (Skaggs et al., 2006).

2.4. Soil-Hydraulic Parameters and Postwildfire Recovery Curves

Nonlinear functions that describe $\theta(\psi)$ and $K(\psi)$ are required to solve Equation 1. We apply the closed-form expressions of van Genuchten (1980) and Mualem (1976), respectively, given as:

$$\theta(\psi) = \theta_r + \frac{\theta_s - \theta_r}{\left(1 + |\alpha\psi|^n\right)^m} \quad (7)$$

$$K(\psi) = K_s \left(\frac{\theta - \theta_r}{\theta_s - \theta_r} \right)^{\ell} \left[1 - \left(1 - \left(\frac{\theta - \theta_r}{\theta_s - \theta_r} \right)^{\frac{1}{m}} \right)^m \right]^2 \quad (8)$$

where θ_s is the saturated soil-water content (dimensionless), θ_r is the residual soil-water content (dimensionless), α is the inverse of the air-entry ψ (L^{-1}), n is the pore-size distribution index (dimensionless), ℓ is the pore-connectivity parameter (dimensionless) ($\ell = 0.5$; Mualem, 1976), K_s is the saturated hydraulic conductivity (LT^{-1}), and $m = 1 - \left(\frac{1}{n} \right)$ (dimensionless). Reductions in the potential for runoff-generated debris flows as landscapes recover from fire has been linked to the return of the soil saturated hydraulic conductivity (K_s), among other soil-hydraulic parameters, towards prewildfire levels (Ebel, 2020; McGuire et al., 2021). We use two different methods to define how postwildfire infiltration properties for the upper 5 cm of soil can change over the recovery period. First, we use the logistic function proposed by Ebel and Martin (2017):

$$K_s(t_f) = \frac{K_{s_{UL}} K_{s_{LL}} e^{\tau_{K_s} t_f}}{K_{s_{UL}} + K_{s_{LL}} (e^{\tau_{K_s} t_f} - 1)} \quad (9)$$

where t_f is the time since fire (T), $K_{s_{LL}}$ is the minimum value for the K_s immediately after the fire (LT^{-1}), $K_{s_{UL}}$ is the unburned K_s that provides an asymptotic upper limit (LT^{-1}), and τ_{K_s} is a parameter that governs the rate of K_s recovery (T^{-1}). We refer to rainfall thresholds derived using this formulation of $K_s(t_f)$ as field-based thresholds. Second, because field-based estimates of K_s following wildfire are scarce, we also explore the use of the Ebel and Martin (2017) logistic function to relate changes in satellite-based LAI to K_s recovery at the annual timescale. We evaluate the use of LAI because vegetation regrowth may (a) increase root development and bioturbation (Hubbert & Oriol, 2005), promoting macropore flow; (b) increase surface roughness (Canfield et al., 2005; Rengers, Tucker, et al., 2016; Tang et al., 2019a), reducing runoff velocity; and (c) increase canopy cover (Cerdá, 1998), reducing raindrop impact which could otherwise promote surface sealing effects (Larsen et al., 2009). Although we focus here on changes in infiltration on the annual timescale, LAI may be useful for sub-annual timescales, as seasonal fluctuations in soil-water repellency have been linked to patterns in rainfall and soil moisture (Hubbert & Oriol, 2005), which are also factors for vegetation regrowth. To evaluate if LAI recovery is congruent with the Ebel and Martin (2017) logistic function, we extract the mean postwildfire MODIS 8 d LAI from the footprint of a fire and fit the annual postwildfire LAI maxima to a LAI-based version of Equation 9:

$$LAI(t_f) = \frac{LAI_{UL} LAI_{LL} e^{\tau_{LAI} t_f}}{LAI_{UL} + LAI_{LL} (e^{\tau_{LAI} t_f} - 1)} \quad (10)$$

where LAI_{LL} is the minimum value for the LAI immediately after the fire (dimensionless), LAI_{UL} is the unburned LAI that provides an asymptotic upper limit (dimensionless), and τ_{LAI} is a parameter that governs the rate of LAI recovery (T^{-1}). We then linearly transform Equation 10 to relate the limits of $LAI(t_f)$ to the limits of $K_s(t_f)$:

$$K_s(t_f) = \left[K_{s_{UL}} - \left(LAI_{UL} \frac{K_{s_{UL}} - K_{s_{LL}}}{LAI_{UL} - LAI_{LL}} \right) \right] + \left[\left(\frac{K_{s_{UL}} - K_{s_{LL}}}{LAI_{UL} - LAI_{LL}} \right) \left(\frac{LAI_{UL} LAI_{LL} e^{\tau_{LAI} t_f}}{LAI_{UL} + (LAI_{LL} (e^{\tau_{LAI} t_f} - 1))} \right) \right] \quad (11)$$

We refer to rainfall thresholds derived using this formulation of $K_s(t_f)$ as satellite-based thresholds.

2.5. Failure Criteria for Runoff- and Infiltration-Generated Debris Flows

We use the simulated output at annual intervals along the postwildfire recovery timeline as an initial condition to simulate an ensemble of 25 low to high intensity (1–125 mm hr⁻¹) rainfall events lasting up to 24 h (Figure 2a). These event-based simulations, whose results form the basis of our thresholds, are structured around a 24 h period to place our results within the context of rainfall forecasting constraints in the United States, as uncertainty associated with quantitative estimates of precipitation (Novak et al., 2014) are often too great to be meaningful for debris flow hazard predictions more than 24 h in advance. For each event-based simulation we track the runoff rate at the surface and pore-water pressure at the soil-bedrock interface (Figure 2b). We first convert the point-scale runoff rate (Figure 2b) from our hydrologic simulations to a unit discharge (q) (L²T⁻¹) (e.g., Figure 2d; similar to Kean et al., 2016):

$$q = \frac{RA}{W} \quad (12)$$

where R is the water runoff rate, or net flux that does not infiltrate according to our simulations using Equation 1 (LT⁻¹), A is the drainage area above a failure-prone location (L²), and W is the channel width at a failure-prone location (L). We then convert the unit discharge into dimensionless discharge (q^*) with the Gregoretti and Fontana (2008) approach, which has been demonstrated to be suitable for quantifying typical values of q^* during periods dominated by flooding and debris flow activity in our study area (Tang et al., 2019b):

$$q^* = \frac{q}{\sqrt{(G_s - 1)gD_{50}^{1.5}}} \quad (13)$$

where G_s is the specific gravity of the sediment (dimensionless) ($G_s = 2.6$; McGuire & Youberg, 2020; Tang et al., 2019b), g is the acceleration due to gravity (LT⁻²), and D_{50} is the median grain size (L) within the channel. To evaluate if runoff-generated debris flows should be expected, we compare the simulated $q^*(t)$ to a critical dimensionless discharge (q_{crit}^*) that is given by Gregoretti and Fontana (2008) as:

$$q_{crit}^* = \frac{C}{[\tan(\beta_c)]^N} \quad (14)$$

where C and N are empirical coefficients ($C = 4.29$, $N = 0.78$; McGuire & Youberg, 2020; Tang et al., 2019b) to delineate the transition from water-dominated flow to debris flow and β_c is the channel slope at the failure-prone location (°). Runoff-generated debris flows are expected if $q^* > q_{crit}^*$.

To evaluate infiltration-generated debris-flow potential, we convert the ψ from Equation 1 to subsurface pore-water pressure (u_w) (ML⁻¹T⁻²) (Freeze & Cherry, 1979):

$$u_w = \rho g \psi \quad (15)$$

We then calculate the suction stress at the soil-weathered bedrock interface, given by Lu and Godt (2013) as:

$$\sigma^s = -\frac{\theta - \theta_r}{\theta_s - \theta_r}(u_a - u_w) \quad (16)$$

where σ^s is the suction stress (ML⁻¹T⁻²) and u_a is the pore-air pressure (ML⁻¹T⁻²) (assumed equal to the atmospheric pressure, which is zero in reference pressure). To evaluate if infiltration-generated debris flows should be expected, we calculate the factor of safety (FS) with the infinite slope equation (Lu & Godt, 2008):

$$FS = \frac{(c_s + c_r) + [\gamma d \cos^2(\beta_H) - \sigma^s] \tan \phi'}{\gamma d \sin \beta_H \cos \beta_H} \quad (17)$$

where c_s is the cohesion associated with the soil (ML⁻¹T⁻²), c_r is the cohesion associated with the roots (ML⁻¹T⁻²), γ is the bulk unit weight of the soil (ML⁻²T⁻²), d is the vertical depth from the surface to the

failure plane (L), β_H is the hillside slope ($^\circ$), and ϕ' is the effective friction angle ($^\circ$). We hold the geometric and material properties constant, except for the bulk unit weight of the soil (γ) ($\text{ML}^{-2}\text{T}^{-2}$), which is given by Freeze and Cherry (1979) as:

$$\gamma = \gamma_w \frac{G_s + eS}{1 + e} \quad (18)$$

where γ_w is the unit weight of water ($\text{ML}^{-2}\text{T}^{-2}$) ($\gamma_w = 9.8 \text{ kNm}^{-3}$; Freeze & Cherry, 1979), $e = \frac{\theta_s}{1 - \theta_s}$ is the void ratio (dimensionless), and $S = \frac{\theta}{\theta_s}$ is the saturation (dimensionless). Infiltration-generated debris flows are expected if $FS < 1$.

2.6. Delineation of Simulation-Based Thresholds for Postwildfire Debris Flows

Our thresholds for debris flow activity are based on the simulated surface runoff and subsurface pore-water pressure response associated with each rainfall-intensity duration ensemble (Figure 2a). For a given rainfall intensity simulation in the ensemble of 25 rainfall events (which range from 1 to 125 mm hr^{-1}), we note the simulation time (or rainfall duration) when the failure criteria for runoff- and infiltration-generated debris flows (i.e., Equations 14 and 17, respectively) are satisfied. To delineate a threshold, we plot the 25 simulated rainfall intensity and rainfall duration results and connect the points with a simple, piecewise linear interpolation (e.g., Godt & McKenna, 2008; Thomas, Mirus, & Collins, 2018).

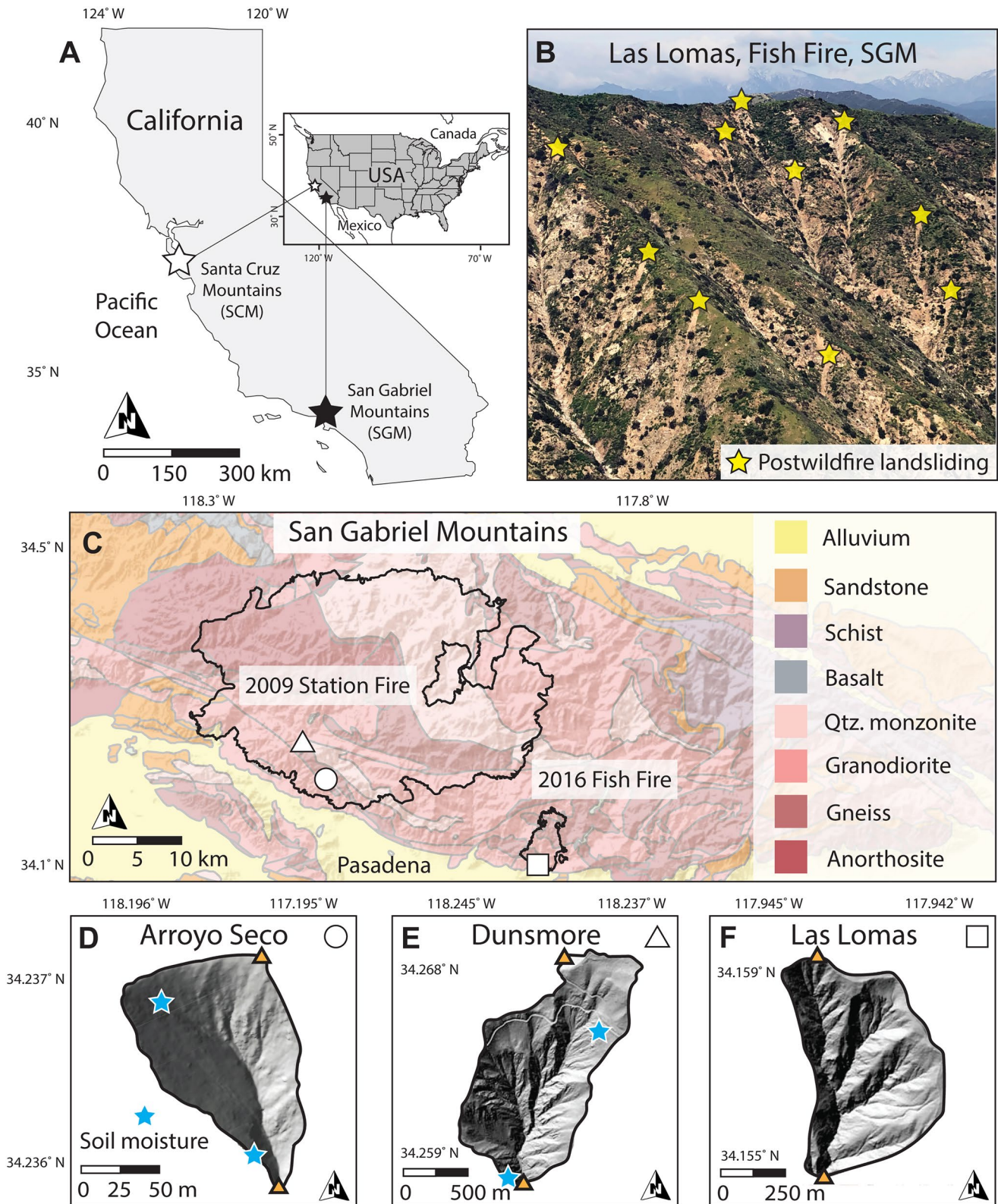
3. Framework Testing and Application

3.1. Regional Context and Hillslope Hydrologic Monitoring Data

We test our threshold simulation framework with hillslope hydrologic and postwildfire debris flow observations from the San Gabriel Mountains in southern California, USA (Figure 3a). This region experiences hot and dry summers followed by cool and wet winters; annual precipitation amounts vary with elevation and aspect, but the lower, developed hillslopes of our study region receive $\sim 650 \text{ mm yr}^{-1}$, predominantly as rainfall (PRISM Climate Group, 2020). Vegetation classes include grasslands, savanna, and shrublands (NASA, 2020a), with drought- and fire-adapted chaparral dominating the landscape (Halsey, 2005). The steep, tectonically active terrain (DiBiase et al., 2010) hosts thin ($\leq 1 \text{ m}$) sandy soils (USDA, 2020) underlain by granitic and metasedimentary rocks (Figures 3b and 3c; Jennings et al., 1977). These rugged slopes, which are in close proximity to the densely populated Los Angeles basin, are well known to produce deadly and destructive postwildfire debris flows (Eaton, 1935; McPhee, 1989).

We use soil moisture observations from two monitoring stations in the San Gabriel Mountains that are operated by the U.S. Geological Survey (Smith et al., 2019) to evaluate the ability of our mathematical representation of hydrologic response to capture fluctuations in daily soil wetness for multi-annual timescales. These stations, which we refer to as “Arroyo Seco” and “Dunsmore,” are located within the footprint of the 2009 Station Fire (Figures 3d and 3e) in steep ($\geq 30^\circ$) and small (0.01 and 0.5 km^2 , respectively) low-order basins that experienced moderate to high soil burn severity (99% and 43% of the basin area, respectively; Kean et al., 2011). Both catchments produced runoff-generated debris flows in the first wet season following wildfire (Kean et al., 2011; Staley et al., 2014). Each site includes two vertical monitoring arrays that were established six years after the fire with three EC-5 dielectric soil-water content sensors (Meter Group, 2020) positioned at 10, 25, and 50 cm depths (for soil profiles that are $\sim 50 \text{ cm}$; Smith et al., 2019) near a drainage divide and a basin outlet (Figures 3d and 3e).

We conduct a suite of numerical simulations to (a) compare our postwildfire threshold development approach to existing observations and empirical thresholds in the San Gabriel Mountains and (b) describe changes in failure criteria throughout the recovery timeline for the 2016 Fish Fire in the “Las Lomas” catchment. Las Lomas is located within the footprint of the 2016 Fish Fire (Figures 3c and 3f) and greater 2016 San Gabriel Complex fires. We apply our simulation framework to the 2016 Fish Fire because this area



experienced runoff- and infiltration-generated debris flows soon after and three years following the fire, respectively (Rengers et al., 2020; Tang et al., 2019a). The setting at Las Lomas is similar to that of Arroyo Seco and Dunsmore, that is, a small low-order basin with steep (38°; Tang et al., 2019a) slopes and thin (average depth = 35 cm; Rengers et al., 2020) sandy soils that experienced moderate soil burn severity (~40% of basin area, respectively; USDA, 2021). Eleven runoff-generated debris flows were observed at the Las Lomas watershed outlet over the course of seven rainstorms in the first year after the fire (Kean, Smith, et al., 2019; Tang et al., 2019a). In addition, the area within and around the Fish Fire burn scar produced several hundred shallow landslides of the debris slide-debris flow type (Varnes, 1978) in response to a single, long-duration rainstorm during the third year following the fire (Figure 3b; Rengers, 2020). These shallow landslides, whose failure planes generally corresponded with the interface between soil and weathered bedrock, were concentrated on recently burned south-facing slopes, although some did occur in nearby unburned areas (Rengers et al., 2020). The observed transition in mass wasting types following the 2016 Fish Fire (McGuire et al., 2019; Rengers et al., 2020) provides a timely opportunity to explore how postwildfire soil-hydraulic recovery affects rainfall intensity-duration thresholds.

3.2. Evaluating the Physical Representation and Parameterization of Hillslope Hydrologic Response

3.2.1. Variably Saturated Subsurface Flow

Our focus is on using event-scale simulation to evaluate debris flow hazard potential when the short timescale when vertical infiltration dominates the slower processes of lateral subsurface distribution (Iverson, 2000). Accordingly, we use the one-dimensional (1-D) form of the Richards (1931) equation. Solving the 1-D Richards equation reduces the computational burden, convergence issues, and intensive parameterization demands associated with the multi-dimensional form of the non-linear partial differential equation. Steep terrain, however, is subject to seasonal transitions between locally controlled and topographically controlled soil moisture states (Grayson et al., 1997). To evaluate whether 1-D simulation types could capture fluctuations in daily soil wetness for multi-annual timescales in our study region, we compare the simulated output from the satellite-based recovery timeline to soil moisture observations from the Arroyo Seco and Dunsmore monitoring sites.

We use the U.S. Department of Agriculture (USDA) Rosetta software package (Schaap, 1999) to define the soil-hydraulic parameters for loamy sand ($\theta_s = 0.39$; $\theta_r = 0.05$; $\alpha = 0.35 \text{ mm}^{-1}$; $n = 1.75$; $K_s = 43.8 \text{ mm hr}^{-1}$), which is the predominant soil texture throughout our study region (USDA, 2020). We allow water uptake in the upper 75% of the 50 cm thick soil mass, as this was the average rooting depth exposed by postwildfire shallow landsliding in the San Gabriel Mountains (Rengers et al., 2020), although individual roots can vertically penetrate the underlying weathered rock in this region (Halsey, 2005). We assume identical hydraulic properties for the underlying weathered bedrock, with the exception of the K_s , which we set as two orders of magnitude lower than that of the soil, and the θ_s , which we set to half that of the soil (Katsura et al., 2009). In the absence of repeat postwildfire field measurements of the soil K_s for Arroyo Seco and Dunsmore, we use the satellite LAI-based recovery model (Equation 11) to define the K_s recovery curve. We assume a $K_{s_{UL}}$ equal to the K_s for a loamy sand (43.8 mm hr^{-1} ; Schaap, 1999) and a $K_{s_{LL}}$ equal to 16.2 mm hr^{-1} based on a ratio of burned to unburned K_s equal to 0.37, as suggested for use with postwildfire infiltration models in southern California (Ebel & Moody, 2020). The 16.2 mm hr^{-1} K_s value is similar to the median value of K_s (17 mm hr^{-1}) measured less than three months after the start of the Fish Fire (McGuire et al., 2021), but is greater than K_s values inferred from event-based simulations of runoff at the catchment scale in the first wet season following the Station Fire, which ranged from 1 to 10 mm hr^{-1} (Rengers et al., 2016).

Figure 3. (a) Index map showing the location of the San Gabriel Mountains (SGM) and Santa Cruz Mountains (SCM) in California, USA. (b) Photograph of infiltration-generated shallow landslides that transitioned into debris slides and debris flows in the third year following the Fish Fire (Rengers, McGuire, Oakley, et al., 2020). Photograph by Francis Rengers, U.S. Geological Survey. (c) Shaded relief and geologic map (USGS 2020b) of the SGM showing the footprint of the 2009 Station Fire and 2016 Fish Fire. The white circle, triangle, and square indicate the location of (d) Arroyo Seco, (e) Dunsmore, and (f) Las Lomas sites. The blue stars in (d)–(e) correspond to the “upslope” and “downslope” soil moisture monitoring arrays (Smith et al., 2019) that we use to evaluate our multi-annual simulation framework (Figure 2). We adapted the hillshade catchment maps in (d)–(f) from Tang et al. (2019b). The orange triangles in (d)–(f) correspond to the minimum and maximum elevations of each site.

Table 1
Summary of Input Parameters That We Use to Define Field-Based Recovery Curves (Equation 11) for Surface Soil Saturated Hydraulic Conductivity Following the 2016 Fish Fire

Field-based curve ^a	Input parameters for logistic function			Satellite- versus field-based Ks curve
	Ks _{LL} (mm/hr)	Ks _{UL} (mm/hr)	r _{Ks} (yr ⁻¹)	R ²
Upper bound	25.5	87.5	4.86	0.77
Median	12.9	19.5	13.63	0.29
Lower bound	0.5	5	3.21	0.99
Overall average	13	37.5	4.47	0.79

Ks_{LL} = saturated hydraulic conductivity, lower limit.

Ks_{UL} = saturated hydraulic conductivity, upper limit.

r_{Ks} = parameter governing rate of Ks recovery.

R² = coefficient of determination.

^aSee Figure 6c for boxplots of tension infiltrometer data.

The EC-5 soil moisture sensors at Arroyo Seco and Dunsmore are not calibrated to the local soil type, so we compare the normalized mean daily soil wetness (θ_n (dimensionless)); similar to the effective saturation in van Genuchten, 1980) to the recovery simulation output for January 1, 2016 through January 1, 2020:

$$\theta_n = \frac{\theta - \theta_{\min}}{\theta_{\max} - \theta_{\min}} \quad (19)$$

where θ_{\min} (dimensionless) and θ_{\max} (dimensionless) are, respectively, the minimum and maximum volumetric soil-water content. The timeline of available observations is valuable in that the comparison integrates the impacts of uncertainty in the flow model physics (1-D Richards (1931) equation), environmental inputs (daily rainfall, air temperature, and LAI), and parameter value choices (domain geometry, hydraulic properties, satellite-based Ks recovery curve) on hydrologic response through postwildfire simulation phases.

3.2.2. Surface Runoff

The expression that we use to evaluate the potential for runoff-generated debris flows (Equation 13) requires an estimate of the time-varying unit discharge (q). We scale our 1-D simulation results by a contributing area and channel width to convert the point-scale runoff rates into a quasi-distributed estimate of q (Equation 12). To evaluate if this method could approximate q at the Arroyo Seco site for conditions soon after the Station Fire, we compare our quasi-distributed estimates of q that do not account for flow routing times to those based on a fully distributed simulation of flow routing with a kinematic wave model whose parameterization has been applied to postwildfire settings in southern California (Rengers, McGuire, et al., 2016, Rengers et al., 2019). The A , W , and β_c values that we selected for Arroyo Seco ($A = 4500 \text{ m}^2$, $W = 1.5 \text{ m}$, and $\beta_c = 33^\circ$) are based on interpretations of slope-area relationships where postwildfire runoff-generated debris flows were observed (Staley et al., 2014). Specifically, we base the A on the hillslope to channel transition point and measured the W and β_c from a digital elevation model at that point (Staley et al., 2014). We first simulate 1-D runoff response for 5, 10, 15, 30, and 60 min rainfall intensities with recurrence intervals ranging from 1 to 100 years (e.g., a 5 min rainstorm with a constant intensity equal to the one-year recurrence interval) and then apply the resulting runoff rates as inputs to the kinematic wave model to track the simulated q for the failure-prone location (see white star in Figure 2d). For the kinematic wave model, we estimate the hillslope roughness using a D_{50} particle size for conditions soon after the wildfire ($6.3 \times 10^{-4} \text{ m}$; Tang et al., 2019b) and then use the hillslope roughness to determine a Manning roughness coefficient. We estimate the channel roughness using a D_{84} particle size ($1.2 \times 10^{-2} \text{ m}$; Rengers et al., 2019) and use the channel roughness as an input into a variable-power equation (Ferguson, 2007) to control flow velocity within channels.

3.2.3. Fire-Affected Soil Saturated Hydraulic Conductivity

A quantitative and continuous representation of how infiltration properties can change as a function of time is a key component of our numerical simulation framework. Although it has been long recognized that wildfire can reduce infiltration potential (e.g., Parks & Cundy, 1989), relatively few in situ measurements of Ks recovery have been made to constrain this behavior. Therefore, we test how globally available satellite-based measurements of vegetation reflectance (NASA, 2020b) compare to Ks measurements that were derived using repeat tension infiltrometer measurements following the 2016 Fish Fire (McGuire et al., 2021). We fit the outermost bounds and median of the field-based Ks recovery measurements (Figure 6c; Table 1) to Equation 9 using a non-linear least squares approach. We favor the use of a simple, monotonically increasing function because changes in distributions of Ks measurements over the postwildfire monitoring period are statistically insignificant, but the mean and median Ks increase substantially (i.e., 80% and 65%, respectively; McGuire et al., 2021).

3.3. Simulation-Based Thresholds for Postwildfire Runoff- and Infiltration-Generated Debris Flows

We first produce rainfall-intensity thresholds for runoff-generated debris flows for conditions immediately after the Fish Fire (i.e., time since fire is equal to zero) using a field- and satellite-based K_s recovery curve. The contributing area and channel characteristics that we use here ($A = 4500 \text{ m}^2$; $W = 1.75 \text{ m}$, $\beta_c = 34^\circ$) were estimated for the Fish Fire using the same slope-area relationships we applied to the 2009 Station Fire. We compare the simulation-based thresholds to existing 15, 30, and 60 min empirical thresholds for the San Gabriel Mountains (Staley et al., 2017). We also compare the thresholds with observed rainfall intensities during the seven rainstorms that initiated runoff-generated debris flows in the first year following the Fish Fire (Tang et al., 2019a). We then produce a threshold for infiltration-generated debris flows for conditions three years after the Fish Fire using a field- and satellite-based K_s recovery curve. Shear strength testing following ASTM D7608 (ASTM International, 2018) indicates the hillslope soils at Las Lomas have a $c_s = 0 \text{ kPa}$ and $\phi' = 32.7^\circ$. Previous work in the chaparral-dominated hillslopes of the Transverse Ranges suggest that the average for this region is 0.5 kPa and ranges up to 3 kPa (Terwilliger & Waldron, 1990, 1991). For simplicity, we focus on the simulated effects of postwildfire changes to infiltration and therefore assume constant mechanical properties. Following these initial simulations, we determine the lower bound value of the saturated hydraulic conductivity and antecedent soil saturation, respectively, needed to capture both the existing empirical thresholds for runoff-generated debris flows in the first year following fire and shallow landslide observations in the third year following the fire. These adjustments encompass the parametrization for our simulations that define thresholds for runoff- and infiltration-generated debris flows at annual increments along the postwildfire recovery timeline.

4. Results

4.1. Evaluating the Physical Representation and Parameterization of Hillslope Hydrologic Response

4.1.1. Variably Saturated Subsurface Flow and Surface Runoff

Our comparison of measured and modeled soil wetness indicates that a 1-D treatment of Richards (1931) equation that is forced with daily atmospheric and vegetation index timeseries and parameterized with a satellite-based recovery curve can capture fluctuations in daily soil wetness 6–10 years after the 2009 Station Fire (Figure 4a). The modeled values are correlated ($R^2 = 0.87\text{--}0.90$) with observations near the drainage divide and basin outlet (i.e., “Upslope” and “Downslope” locations; Figures 4b–4e) for the Arroyo Seco and Dunsmore monitoring sites. Overall, the simulations appear to slightly underpredict soil wetness. We also find that our quasi-distributed estimates of q , which are based on a 1-D water runoff rate, contributing area, and channel width exhibit a nearly one-to-one relationship with those based on flow routing with the kinematic wave approach (Figure 5). This simulated behavior is consistent for rainfall intensities with recurrence intervals ranging from 1 to 100 years (Figure 5), although the difference is more apparent for the shorter (e.g., 5 min) rainfall durations.

4.1.2. Fire-Affected Soil Saturated Hydraulic Conductivity

The MODIS 500 m 8 d product (NASA, 2020b) is based on radiative transfer modeling that is informed by reflectance data, sun-sensor geometry information, and a land cover model. The long-term prewildfire monthly mean LAI for the 2009 Station Fire (Figures 6a) and 2016 Fish Fire (Figure 6b) exhibits distinct seasonality, with minima during winter dormancy and maxima during the spring green up. The postwildfire LAI shows a similar trend but with consistently reduced magnitudes in the first three years following the fire. The difference between the prewildfire and postwildfire LAI (i.e., the shaded region in Figures 6a and 6b) is greatest immediately after the fire. Variability in the difference between prewildfire and postwildfire LAI for the first year is primarily associated with the vegetation consumed in the fire, but after three years the canopy variability is likely driven by seasonal weather patterns (e.g., rainfall and air temperature) that affect vegetation growth. A model of LAI using Equation 10 correlates with the observed postwildfire annual maxima ($R^2 = 0.61$ and 0.91 for the Station Fire and Fish Fire, respectively), suggesting that it may be possible to estimate the postwildfire green-up process with these data. Field-based estimates of the postwildfire K_s recovery at the Fish Fire show marked variability (Figure 6c). Our three fits of the field-based

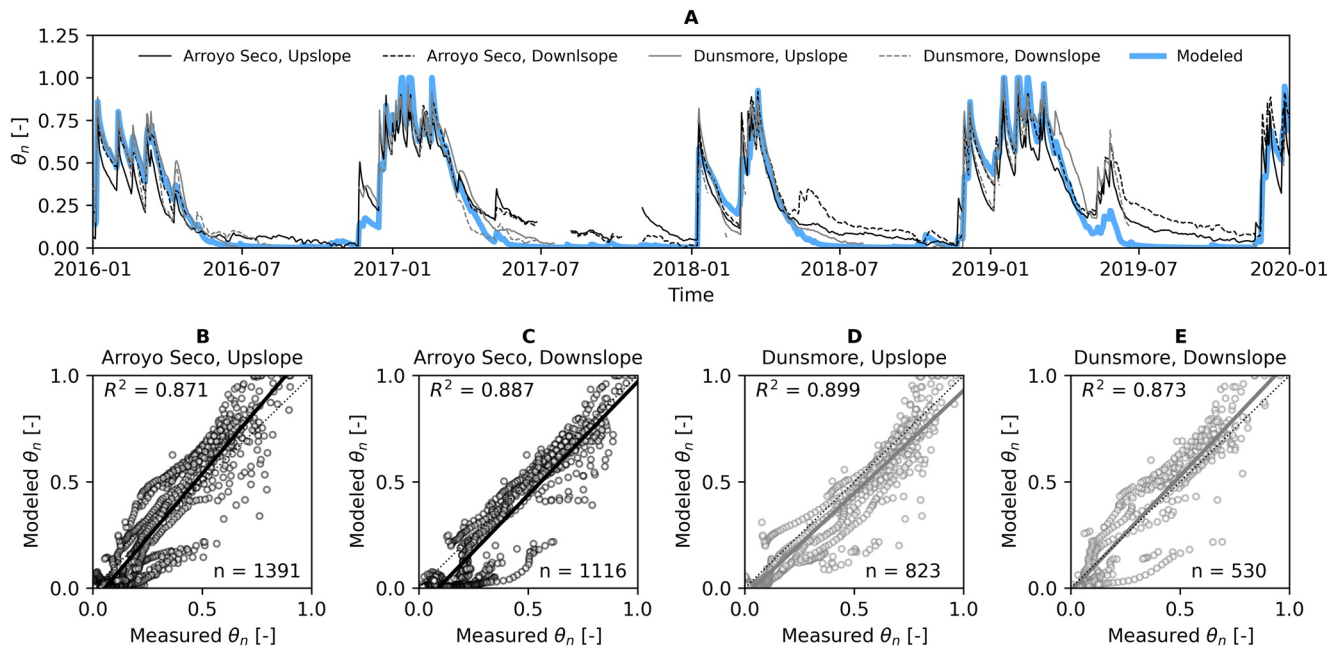


Figure 4. (a) Timeseries of measured and modeled normalized mean daily volumetric soil-water content (θ_n). The measured values are based on the average of sensors positioned at 10, 25, and 50 cm depths. We source θ_n the measurements from EC-5 sensors (Meter Group 2020) installed at the Arroyo Seco and Dunsmore monitoring sites (Figures 3D and 3E). Each site includes a vertical monitoring array near the basin drainage divide (i.e., “Upslope”) and the basin outlet (i.e., “Downslope”). We report the coefficient of determination (R^2) for measured versus modeled θ_n at the Arroyo Seco and Dunsmore sites in (b)-(c) and (d)-(e), respectively. The dashed line indicates 1:1 correspondence (i.e., a perfect fit).

Ks data exhibit weak to strong correlation to the satellite-based curve (i.e., Equation 11; $R^2 = 0.29$ – 0.99 ; Table 1), with the overall average field-based curve showing a correlation with $R^2 = 0.79$. The field-based curves exhibit an earlier Ks recovery than the satellite-based curve, as well as a lower K_{sUL} (i.e., solid vs. dashed lines in Figure 6c).

4.2. Simulation-Based Thresholds for Postwildfire Runoff- and Infiltration-Generated Debris Flows

The field- and satellite-based parameterizations of near-surface hydrologic recovery (Equations 10 and 11) result in thresholds that similarly overestimate the rainfall characteristics that are needed to produce

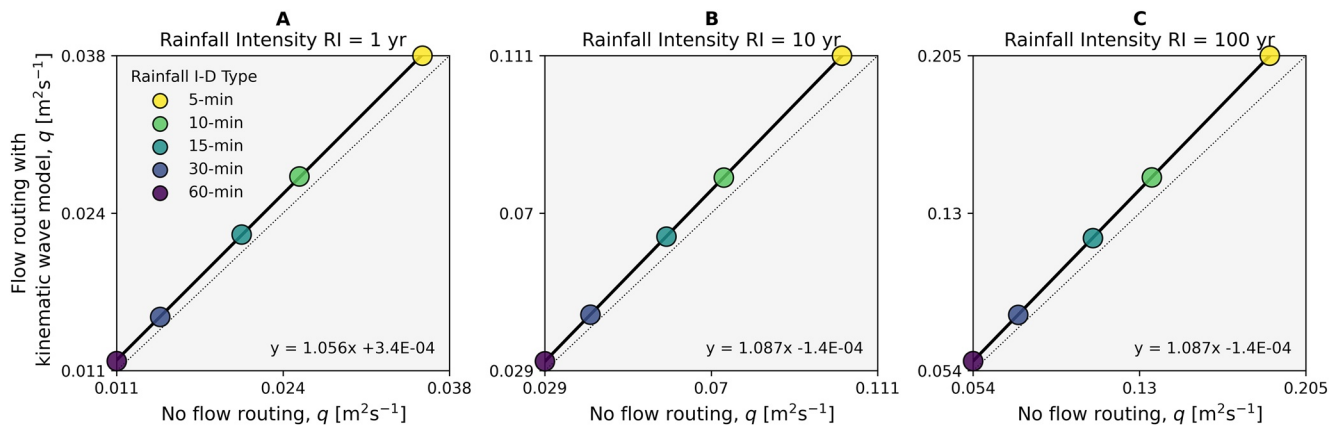


Figure 5. Comparison of simulated peak unit discharge (q) for Arroyo Seco based on flow routing with a kinematic wave model (Rengers, McGuire, et al., 2016) and our 1-D simulations of the runoff rate scaled by a contributing area and channel width for 5-, 10-, 15-, 30-, and 60 min rainfall intensities across (a) 1-, (b) 10-, and (c) 100-year recurrence intervals (RI). The dashed line indicates 1:1 correspondence (i.e., a perfect fit).

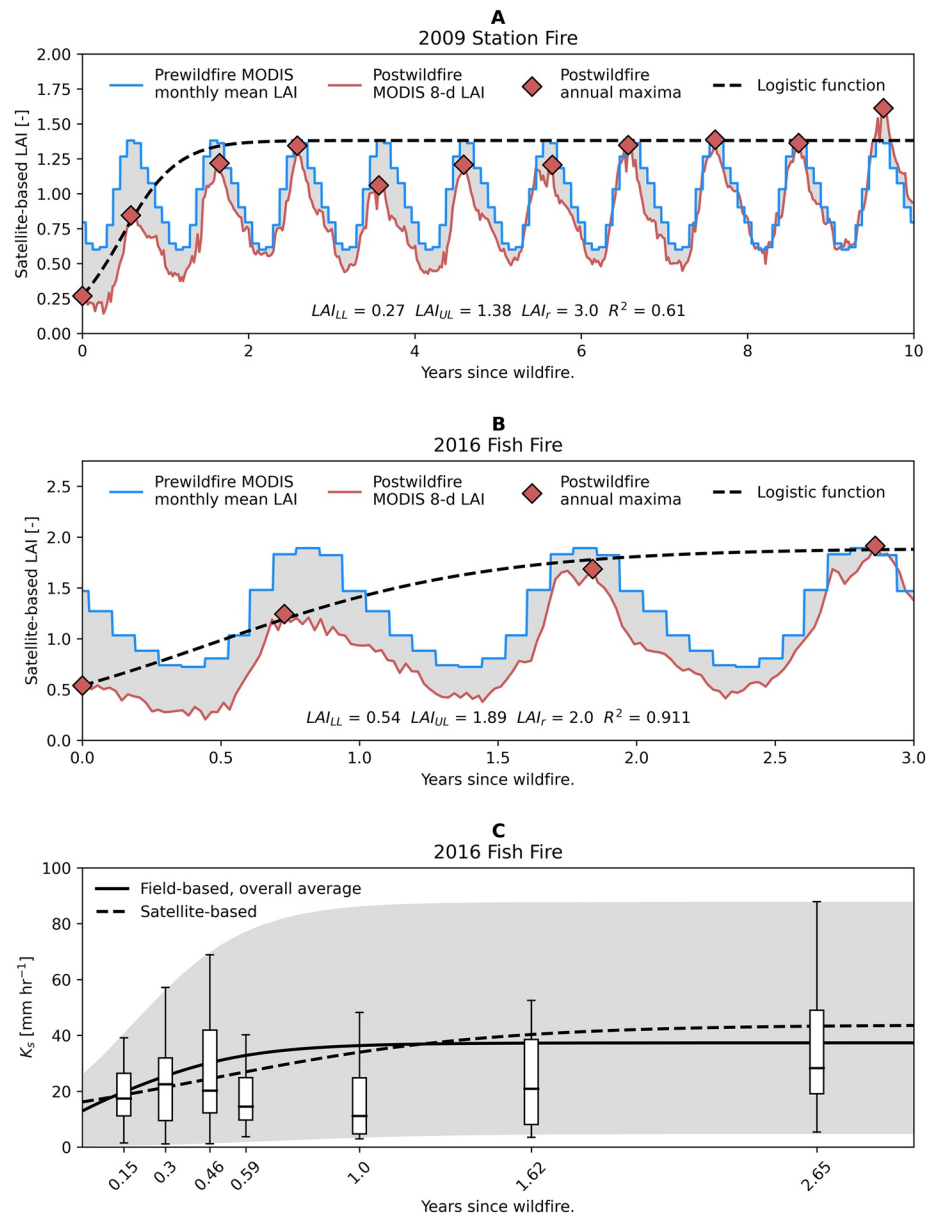


Figure 6. Long-term prewildfire average monthly (blue line) and postwildfire 8 d (red line) National Aeronautics and Space Administration (NASA) Moderate Resolution Imaging Spectroradiometer (MODIS) leaf area index (LAI) timeseries for the (a) 2009 Station Fire and (b) 2016 Fish Fire. The gray shaded area indicates the difference in vegetative reflectance between the long-term average and years following the fire. We fit a logistic function to the postwildfire annual maxima (red diamonds). (c) Field- (solid line) versus satellite-based (dashed line) recovery curves for the surface soil saturated hydraulic conductivity (K_s) for the 2016 Fish Fire. The field-based K_s curve (Equation 9) is the overall average of three fits to the boxplot data (Table 1) derived from repeat tension infiltrometer data. The satellite-based curve is a linearly transformed version (Equation 11) of the recovery curve (Equation 10) shown in (a). The gray shading encompasses the bounds of the field-based K_s boxplots.

postwildfire runoff-generated debris flows in the San Gabriel Mountains (black triangles in Figure 7a), including for the Fish Fire area (white triangles in Figure 7a). However, when we lower the K_{sLL} to 1 mm hr⁻¹ (a value within the range shown in Figure 6c and similar to calibrated postwildfire values for watershed-scale simulations of surface runoff; Rengers, McGuire, et al., 2016), we find that the resulting satellite-based threshold shows agreement with the regional empirical thresholds and correctly predicts debris flow initiation in nearly half of the cases where runoff-generated debris flows were generated in

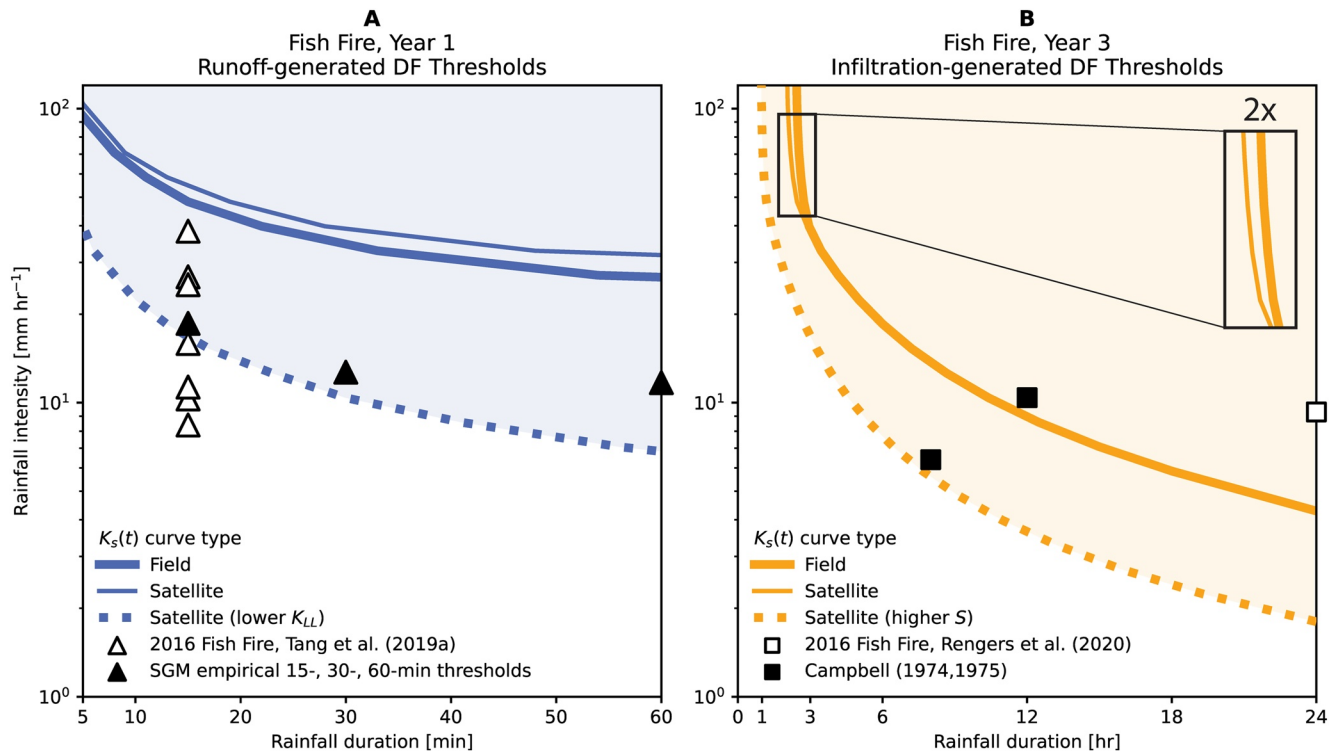


Figure 7. Simulation-based rainfall intensity-duration thresholds for (a) runoff-generated debris flows (DF) for Year 1 following the 2016 Fish Fire and (b) infiltration-generated DF for Year 3 after the 2016 Fish Fire. The thick and thin lines indicate thresholds that we interpolate from simulations using field- and satellite-based soil saturated hydraulic conductivity (K_s) recovery models (Equations 10 and 11). The dashed line in (a) is a satellite-based threshold wherein we adjust the minimum value for the $K_s(K_{sLL})$ until we capture empirical thresholds for postwildfire runoff-generated DF for three durations (black triangles) in the San Gabriel Mountains (SGM). We also compare these thresholds to seven rainstorms that initiated runoff-generated DF in Year 1 following the Fish Fire (white triangles; Tang et al., 2019a). The dashed orange line in (b) is a satellite-based threshold for which we conduct our event-based simulations with a higher antecedent soil saturation (S) to capture historical observations of shallow landsliding (solid black squares) in the Transverse Ranges of southern California (Caine, 1980; Campbell, 1974, 1975) and a rainstorm that initiated several hundred shallow landslides in Year 3 following the Fish Fire (solid white square; Rengers, McGuire, Oakley, et al., 2020). Note: The inset in (b) is a two-times (2x) magnification of the postwildfire thresholds for infiltration-generated DF in high intensity/short duration space. Beyond a rainfall duration of approximately three hours, the field- and satellite-based thresholds overlap.

the first year following the Fish Fire (dotted line in Figure 7a). This adjustment may reflect that K_s is scale dependent in a way that is leading to higher than expected thresholds with our current parameterization approach (Langhans et al., 2016; McGuire et al., 2018; Smith & Goodrich, 2000). The effective K_s , for example, has shown to be lower than the average K_s in burned areas with spatially heterogeneous K_s (McGuire et al., 2018). It is also possible that extensive exposures of bedrock and saprolite could lead to a higher proportion of low K_s sources. The field- and satellite-based parameterizations produce infiltration-generated debris flow thresholds (Equation 17) for Year 3 that are characterized by moderate-intensity, moderate-duration rainfall ($>20 \text{ mm hr}^{-1}$ for $<6 \text{ h}$) and low-intensity, long-duration rainfall ($<10 \text{ mm hr}^{-1}$ for $>12 \text{ h}$; Figure 7b). Slight differences between the field- and satellite-based thresholds can be attributed to the K_{sUL} values (i.e., 37.5 vs. 43.8 mm hr^{-1} , respectively; Figure 6c). These thresholds capture postwildfire shallow landsliding observations for Year 3 in the Fish Fire burn area (Rengers et al., 2020) and one of two historical rainfall observations of widespread rainfall-induced shallow landsliding for unburned conditions in the greater Transverse Ranges (Figure 7b; Campbell, 1974, 1975). We pair the Year 3 Fish Fire observations with the historical landslide observations because shallow landslides were observed inside and outside the Fish Fire burn area and the K_s level in Year 3 is nearly recovered to the K_{sUL} (Figure 6c). When we increase the antecedent soil saturation to 60% and the K_{sLL} to 3 mm hr^{-1} , which is close to the lower end of the 95% confidence interval for observed wildfire reductions in (Ebel, 2019), we found that the resulting satellite-based threshold captures the second historical landsliding observation (dotted line in Figure 7b), as well as the empirical postwildfire runoff-generated debris flow thresholds for the San Gabriel Mountains.

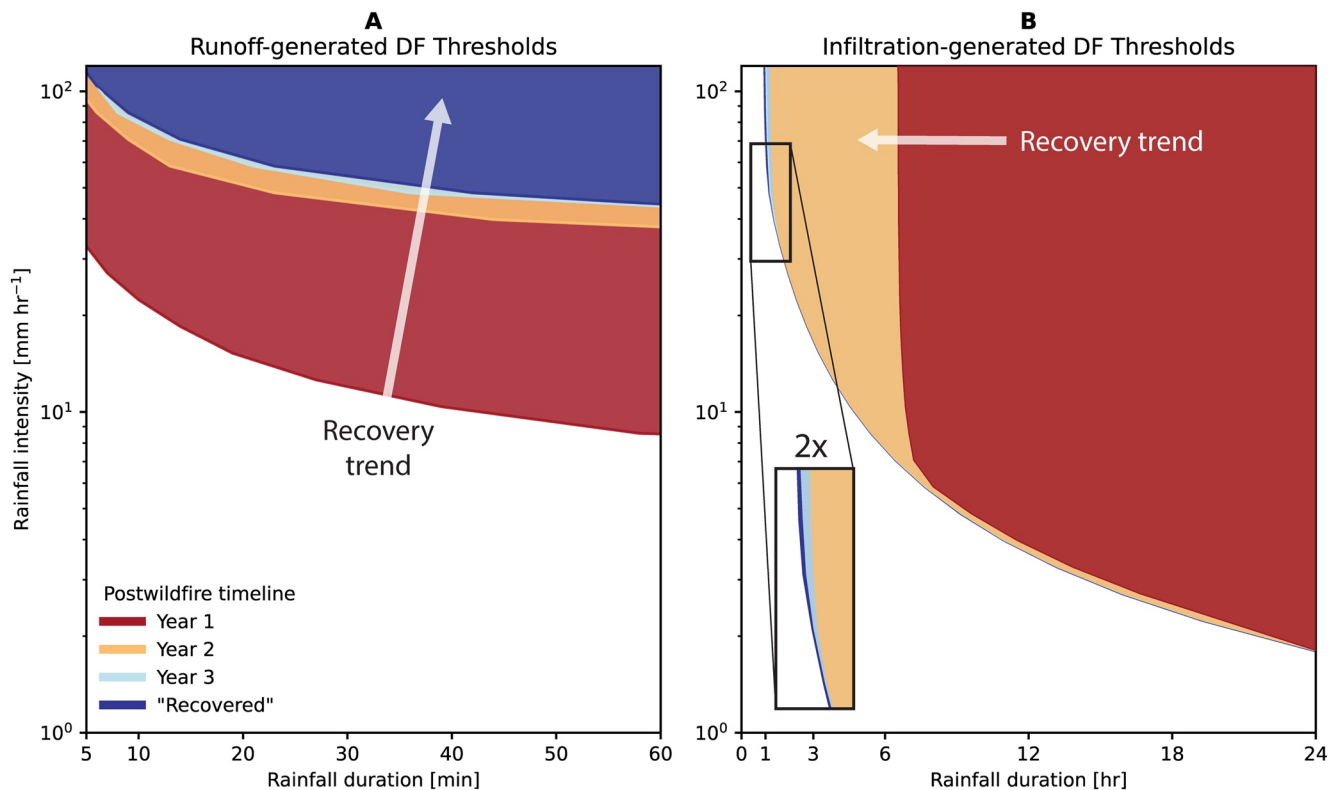


Figure 8. Simulation-based rainfall intensity-duration thresholds for (a) runoff-generated debris flows (DF) and (b) infiltration-generated DF following the 2016 Fish Fire in the San Gabriel Mountains that we interpolate from simulations using a satellite-based soil saturated hydraulic conductivity (K_s) model (Equation 11). The red, orange, and light blue shading indicate the range of rainfall intensity-duration thresholds for Year 1, 2, and 3 following the fire, respectively. The dark blue shading indicates threshold conditions for Year 4, which, for our satellite-based recovery curve, approximates “recovered” conditions. Note: The inset in (b) is a two-times (2x) magnification of the postwildfire thresholds for infiltration-generated DF in high intensity/short duration space. Beyond a rainfall duration of approximately one hour, the Year 2, 3, and 4 thresholds overlap.

The postwildfire runoff- and infiltration-generated debris flow observations for the Fish Fire provide information that bookend the timeline of our threshold simulation framework. Following initial parameter adjustments based on these observations, we simulate rainfall-intensity thresholds for both debris flow initiation mechanisms at annual increments throughout the postwildfire recovery timeline. The most appreciable changes in hazard potential for both debris flow generation mechanisms occur during Year 1 and 2 (Figure 8). The postwildfire runoff-generated debris flow thresholds move upward (i.e., toward higher intensities) in rainfall-intensity duration space during recovery (Figure 8a). This trend reflects the increase of the fire-affected soil K_s through time (Figure 6c). The infiltration-generated debris flow thresholds shift leftward (i.e., toward lower durations) in rainfall intensity-duration space for intensities $>5 \text{ mm hr}^{-1}$ and durations $<8 \text{ h}$ (Figure 8b). As the fire-affected soil K_s increases with time, the barrier to pore-water pressure development at the soil-weathered bedrock interface is less. Whereas Cannon et al. (2008) estimated a relatively uniform, factor of 2 increase between their empirical 15, 30, and 60 min thresholds for runoff-generated debris flows for Year 1 and 2 when they combined data from a fire in the San Gabriel and San Bernardino Mountains, we find that the difference between our Year 1 and Year 2 thresholds is nonuniform (Figure 8a).

5. Discussion

5.1. Probability of Postwildfire Debris Flow Generation Processes

In this study we develop and test a framework for estimating how postwildfire soil-hydraulic recovery translates into time-variable rainfall thresholds. Because our simulation approach permits us to calculate thresholds for multiple debris flow triggering processes, a natural next step is to assess when, in the time since

wildfire, one triggering mechanism may have a higher probability than the other (e.g., Figure 1a). Here, we leverage our modeling framework to explore how rainfall intensity-duration-frequency (IDF) characteristics (i.e., the recurrence interval of rainfall), combined with variability in soil moisture, grain size, and root reinforcement, can influence debris flow likelihood throughout the recovery timeline.

5.1.1. Runoff- Versus Infiltration-Generated Debris Flows

We use National Oceanic and Atmospheric Administration (NOAA) Atlas 14 rainfall IDF data (NOAA, 2020) to determine the recurrence intervals of the rainstorms that define our thresholds. The inverse of the rainfall recurrence interval is the annual probability of a given storm occurring (e.g., a 100 y storm has a 1 in 100 chance of happening in any given year). We plot the median annual probability associated with exceeding our postwildfire runoff- and infiltration-generated debris flow thresholds for the Fish Fire (Figure 9a) and fit a linearly transformed error function to these data:

$$P = a \operatorname{erf}(t) + b \quad (20)$$

where **a** and **b** are fitting parameters (dimensionless) and **p** is the median annual probability (dimensionless) (Figure 9a). Much like Staley et al. (2020), we find that the probability of postwildfire runoff-generated debris flows in southern California is initially high, such that rainstorms with recurrence intervals ≤ 1 y (or **p** = 1) can pose a threat; however, this hazard potential subsides within two years. Conversely, the probability of infiltration-generated debris flows is initially low and climbs modestly throughout recovery. The postwildfire hazard potential trajectories are not symmetric (Figure 9a), as shown in our original conceptual model (Figure 1a) and suggest that fire-induced changes to the soil alone may not be sufficient to impact the median annual probability of postwildfire shallow landsliding potential (McGuire et al., 2019). Loss of root cohesion via root decay following wildfire is widely recognized (DeGraff, 2018; Gehring et al., 2019; Jackson & Roering, 2009; Regelbrugge & Conard, 1993), but a broadly applicable expression that describes its change over time has not been developed. Efforts to quantify temporal changes in root cohesion, which may vary nonmonotonically with time following fire (as is the case following disturbance from logging, for example, Schmidt et al., 2001) would enhance our ability to predict temporal variations in debris flow thresholds.

5.1.2. Impact of Antecedent Soil Saturation

We find that when we use the simulated output from recovery simulations as an initial condition for rainfall intensity-duration ensembles to produce thresholds at annual recovery increments, the antecedent soil saturation is too dry to capture all of the historical observations of widespread shallow landsliding (Figure 7b). These values are low because wildfires in southern California typically occur in the summer and fall (i.e., the driest time of the year; Figure 4a). We found that increasing the antecedent soil saturation to 60%, rather than relying on a dry-season soil moisture level to approximate an annual-level threshold, improved the agreement of our simulated thresholds with available historical observations because this saturation level is more representative of the wet-winter season when shallow landsliding occurs. The resultant threshold also suggests that 24 mm of rainfall in 24 h can induce shallow landsliding on steep slopes with thin sandy soils and minimal root reinforcement. This sensitivity to relatively small rainfall amounts for wetter antecedent conditions is consistent with work suggesting that wet-season rainfall totals in this region must reach 250 mm before widespread rainfall-induced shallow landsliding can occur (Campbell, 1974, 1975).

To better understand how soil moisture can affect our simulated postwildfire rainfall intensity-duration thresholds, we vary the antecedent soil saturation by $\pm 20\%$ throughout the Fish Fire recovery timeline (Figure 9b). Owing to the initially low values, the median annual debris flow probability for runoff-generated debris flows appears largely insensitive to the antecedent soil saturation immediately after the fire. This behavior is similar to observations from Kean et al. (2011), whose measurements of near-surface hillslope soil moisture ranged from dry to wet during the passage of postwildfire runoff-generated debris flows in southern California. However, in the years after the fire, the probabilities become increasingly sensitive to the antecedent soil saturation for infiltration-generated debris flows. The annual postwildfire recovery thresholds in this study are intended to be broadly representative of near-surface hydrologic conditions that are characteristic of the San Gabriel Mountains. However, our field observations and multi-annual

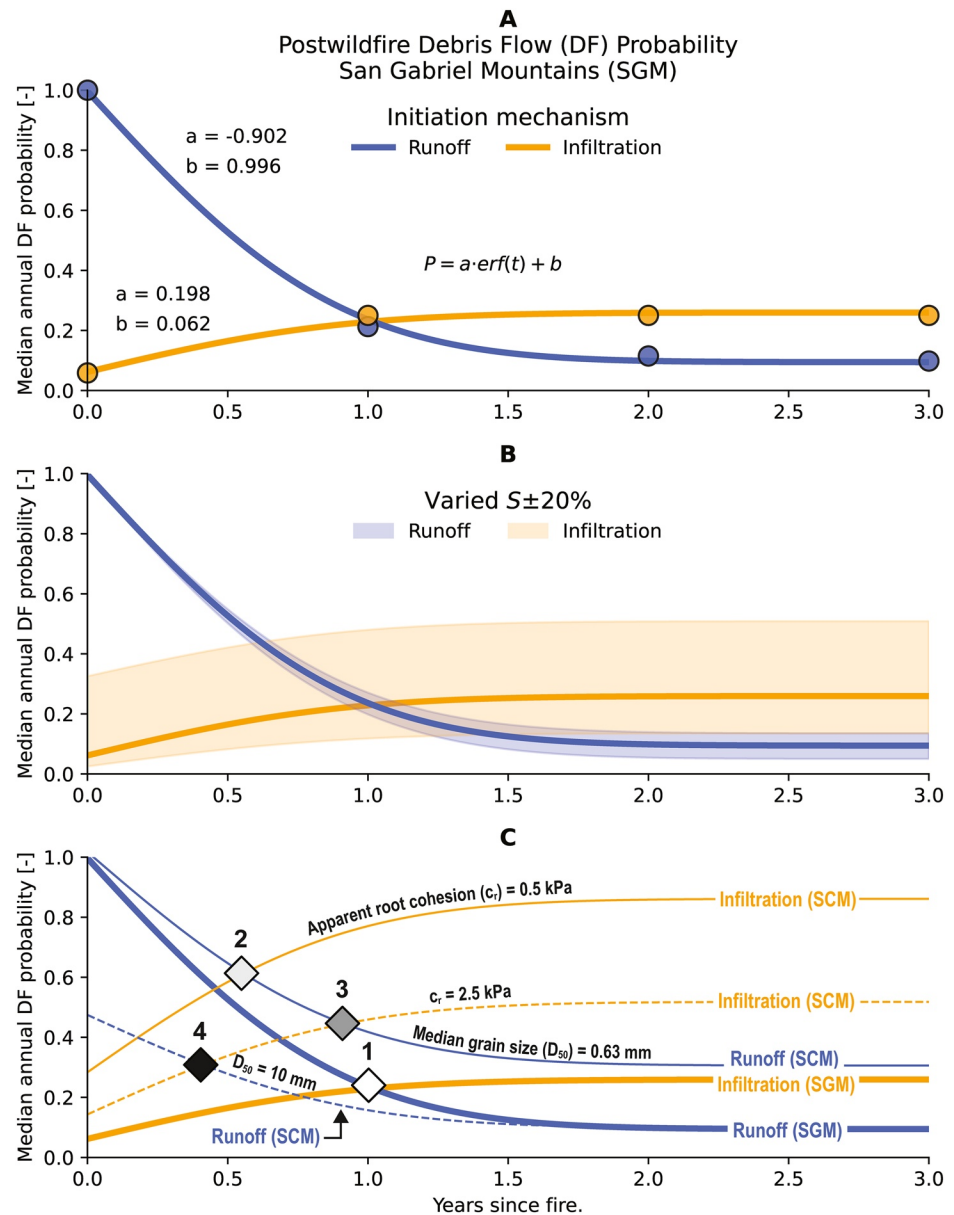


Figure 9. Simulated probabilities of runoff- and infiltration-generated debris flows (DF) following the 2016 Fish Fire in the San Gabriel Mountains (SGM) of southern California (Figure 3A). (a) The median annual DF probability is based on the recurrence intervals of the rainfall intensity-duration-frequency (IDF) characteristics that delineate our simulation-based thresholds (Figure 8). We interpolate between these median annual values using an error function whose coefficients (a and b) are reported for each fit. (b) Illustration of how variations in antecedent soil saturation (S) can affect the simulated trajectories in runoff- and infiltration-generated DF potential. (c) Shifts in the crossover of postwildfire runoff- versus infiltration-generated DF potential (i.e., the white, light gray, dark gray, and black diamonds; see also, Figure 1A) when we use rainfall IDF characteristics for the Santa Cruz Mountains (SCM) in northern California (Figure 3A) as well as a median grain size (D_{50}) and an apparent root cohesion (c_r) that is more representative of small upland forested catchments like the SCM.

climatological and recovery simulations resolved at the daily level, indicate that soil moisture may drive sub-annual variability in rainfall thresholds that does not follow the monotonic trends that we project at the annual level (Figure 8), highlighting the utility of using soil moisture as a normalizing factor when interpreting rainfall-only thresholds for postwildfire soil-hydraulic recovery.

5.1.3. Regional Factors

The methodology that we present in this study to calculate rainfall thresholds for debris flow potential in the years after wildfire is anchored by and tested with observations in southern California, a region where the “fire-flood sequence” has long been recognized as a threat to human lives and property (Kotok & Kraebel, 1935). However, considerably fewer observations are available to delineate the rainfall characteristics that generate postwildfire debris flows in other mountainous regions of the United States (Staley et al., 2017). The Santa Cruz Mountains of northern California (Figure 3a), which are known to produce shallow landslides that transition into debris flows for unburned conditions (Wieczorek et al., 1988), for example, were recently burned by the 2020 CZU Lightning Complex fires. Little information has been collected in this part of the country to support postwildfire debris flow hazard assessment (CGS, 2020) and the extent to which fire will affect debris flow susceptibility here is an open question. Like the San Gabriel Mountains, the Santa Cruz Mountains are characterized by steep, tectonically active terrain that includes granites (Jennings et al., 1977) which produce thin (≤ 1 m) sandy soils (USDA, 2020). Seasonal precipitation patterns for these two regions are similar in that most occurs as rainfall in the winter months; however, the average annual rainfall in the Santa Cruz Mountains (1500 mm yr^{-1}) is approximately twice that of the San Gabriel Mountains (PRISM Climate Group, 2020). Both areas are characterized by diverse vegetation, but the wetter conditions in the Santa Cruz Mountains host temperate rainforests that contrast with the chaparral that dominate the lower, developed hillslopes of the San Gabriel Mountains.

To gain some insight as to how variability in rainfall climatology, grain size, and root reinforcement may affect debris flow hazard following wildfire, we calculate the median annual postwildfire debris flow probabilities for the Fish Fire (San Gabriel Mountains) with NOAA Atlas 14 rainfall IDF characteristics (NOAA, 2020) from the CZU (Santa Cruz Mountains). We also apply a median grain size ($D_{50} = 10 \text{ mm}$; Brummer & Montgomery, 2003) and an apparent root cohesion ($c_r = 2.5 \text{ kPa}$; McGuire et al., 2016; Schmidt et al., 2001) that is more representative of forested terrain like the Santa Cruz Mountains. The resulting postwildfire hazard potential trajectories are notably different (Figure 9c). The Santa Cruz Mountains IDF characteristics suggest runoff-generated debris-flow potential should drop off less precipitously and remain more elevated in later years (see thick blue line versus thin blue line in Figure 9c). When we apply the higher D_{50} value, runoff-generated debris-flow potential for the Santa Cruz Mountains is lower than the for the San Gabriel Mountains in the first half of the postwildfire recovery timeline (see thick blue line versus thin dashed blue line in Figure 9c). Infiltration-generated debris-flow potential is higher immediately after the fire and rises more substantially (see thick orange line versus thin orange line in Figure 9c). When we apply the higher c_r value, the infiltration-generated debris-flow potential for the Santa Cruz Mountains is dampened (see thick orange line versus thin dashed orange line Figure 9c). Taken together, these scenarios suggest that, even when soil-hydraulic and geomorphic properties are assumed identical, differences in rainfall climatology, median grain size, and root reinforcement are sufficient to affect the probability of postwildfire debris flow initiation (see white diamond versus light gray, dark gray, and black diamonds in Figure 9c). Another way to think about the exercise we present here is that, for rainfall recurrence intervals ranging from 1 to 1000 years, the 15, 30, and 60 min rainfall intensities for the Santa Cruz Mountains are, on average, 20.7% higher than the San Gabriel Mountains (NOAA, 2020). Kean and Staley (2021), who present a framework to forecast the frequency and magnitude of postwildfire debris flows, show that for the RCP4.5 emissions trajectory, where rainfall intensity is projected to increase in southern California by 18% (i.e., similar in magnitude to the 20.7% value reported above), the probability of at-threshold and major debris flow events should increase. All else being equal, the Santa Cruz Mountains IDF characteristics result in higher debris flow probabilities than the San Gabriel Mountains; however, we also see that a higher D_{50} and c_r and reduce the likelihood. It is important to highlight that the postwildfire probabilities that we present for the Santa Cruz Mountains (Figure 9c) are hypothetical and that factors beyond rainfall characteristics, median grain size, and root reinforcement (e.g., canopy interception, weathering rates, and soil mineralogy) could also influence debris flow likelihood in this area. Regional variability in these factors underscores the challenges associated with resolving the persistence of postwildfire hazards across climatic gradients that are experiencing increased fire activity (Westerling et al., 2006) and are projected to experience marked increases in sedimentation owing to postwildfire hillslope erosion (Sankey et al., 2017).

5.2. Limitations of This Study and Directions for Further Investigation

Our 1-D simulations of variably saturated flow and quasi-distributed calculations of unit discharge show good agreement with available soil moisture observations (Figure 4) and multi-dimensional flow routing based on a kinematic wave model (Figure 5). These results indicate that our dimensionality reduction approach can approximate multi-annual and event-based hillslope hydrologic response characteristics that are relevant to runoff- and infiltration-generated debris flow initiation for small-, low-order hollows in the San Gabriel Mountains. Although we find good coherence between our point-scale soil moisture data and model outputs, it is important to highlight that we focus on coarse-grained sandy soils that are common in the San Gabriel Mountains. Fine-grained soils, for example, may exhibit water retention and hydraulic conductivity characteristics that drive slower rates of vertical infiltration. Furthermore, we have not applied our simulation framework to larger basins. We expect that, beyond a critical contributing area, accounting for flow routing times will be important to accurately delineate rainfall thresholds for runoff-generated debris flows throughout the soil-hydraulic recovery timeline. Partial source area runoff generation in larger basins, whereby most of the runoff is generated from near-channel areas because farther upslope areas that generated runoff have re-infiltrated (e.g., Ebel et al., 2016; Sheridan et al., 2007) could further complicate upscaling our approach. Therefore, future work could focus on multiple soil types, as well as the transferability of the slope-area relationships we use to identify debris flow initiation points and evaluate the maximum basin area for which our approach is valid.

We use a coarse resolution (500 m, 8 d) LAI data product averaged over a burn area to evaluate if remotely sensed changes in vegetative reflectance following wildfire correlate with observations from point-scale tension infiltrometer surveys (Figure 6c). We focus on fitting a logistic function (Equation 10) to this information at roughly annual increments and assume that the reflectance should recover to typical prewildfire levels without normalizing for factors that may affect vegetation growth (e.g., air temperature and rainfall). The pattern of burn severity across fires can, of course, be highly variable, and the types and densities of vegetation do not reestablish in a strictly uniform fashion. However, our test case is for an environment that is well adapted to fire, predominantly hosts grasslands, savannas, and shrublands (as opposed to coniferous or broadleaf forests that are typified by more complex canopy structures) and is not dominated by postwildfire vegetation type conversion (Meng et al., 2014). Differences between the field- and satellite-based K_s could also be related to non-vegetation-related aspects of recovery, such as the coarsening of the hillslope sediment due to loss of fine-grained dry ravel. An important next step could be to quantify postwildfire recovery trends with LAI or other satellite-based vegetation indices (e.g., enhanced vegetation index or the normalized difference vegetation index) for historical fires across a broader range of climate zones, ideally with sufficient spatial resolution (e.g., USGS, 2020a) to evaluate factors such as burn severity and slope aspect.

Whereas we consider the monotonic increase of the surface soil K_s for our simulations, others have observed that the postwildfire soil K_s is not always lower than the prewildfire value (Raymond et al., 2020) and that the water repellent zone can be below the top of the soil surface and of variable thickness (Debano, 1979). Also, postwildfire hydrologic recovery may not occur in a strictly monotonic fashion (Nyman et al., 2014; Shakesby et al., 1993). These complexities emphasize the need to better understand how (or if) sub-annual variability in soil-hydraulic recovery can impact postwildfire recovery thresholds that are geared toward annual timescales. Establishing functional relationships to quantify recovery trends for different landscapes and burn conditions is especially important for postwildfire debris flow hazard assessment, where the recovery trajectories cannot be defined in hindsight, as for our test cases.

The framework we introduce in this study permits time-variable K_s ; however, postwildfire changes to the soil porosity (θ_s), and to a lesser extent, the residual soil-water content (θ_r), air-entry pressure head (α), and pore-size distribution index (n) have also been observed (Ebel & Moody, 2020; Nyman et al., 2014). Variability in soil-hydraulic parameters (beyond the K_s) is known to influence the simulation of pore-water pressure metrics that are relevant to shallow landslide initiation in unburned settings (Ebel et al., 2018; Thomas, Mirus, Collins, Lu, & Godt, 2018), but the relevance of this variability for postwildfire settings and for runoff-generated debris flows is presently unknown. This knowledge gap highlights the need for technological advancements to better characterize vadose zone processes in postwildfire settings. Repeat measurements of the full suite of van Genuchten (1980) soil parameters throughout postwildfire soil-hydraulic recovery,

for example, are needed to further test our modeling framework. Laboratory-based approaches (e.g., Delgado et al., 2020) have shown promise, but in situ measurements of soil suction paired with soil moisture may also be helpful to detect changes in water retention and hydraulic conductivity characteristics. These types of monitoring arrays, which must be able to function in hyper dry through wet soil conditions, should be deployed soon after the fire and maintained for several years to quantify how subsurface hydrologic response to rainstorms changes over time. These measurements could be paired with the logistic function we used in this study (Ebel & Martin, 2017) and would facilitate a better understanding of how temporal variability in soil-hydraulic properties can influence rainfall thresholds for postwildfire debris flow hazard potential.

While we focus on quantifying the impact of soil-hydraulic recovery on the hydrologic triggering conditions for debris flows, we recognize that the hillslope and channel geomorphology can also change during postwildfire recovery. For example, surface roughness may increase with time since fire (Canfield et al., 2005; Rengers, Tucker, et al., 2016; Tang et al., 2019a); however, for our kinematic wave model simulation we hold roughness factors constant because there is currently no systematic approach for estimating this time-variable effect. As a result, our assessment of runoff-generated debris flows is likely conservative because we do not account for decreases in runoff velocity (and therefore, unit discharge) as roughness increases with vegetation growth. We also do not account for the effects of surface erosion. Postwildfire erosion can incise hillslopes on the order of several centimeters (Staley et al., 2014), thereby thinning or removing the fire-affected soil horizon during rainstorms. New work has shown that high-resolution change detection technologies can be useful to monitor inter-rill and rill erosion and that much of this erosion takes place during the first few storms following the fire (Guilinger et al., 2020). Incorporating this process into our simulation framework would require remeshing the finite-element domain as a function of time – a technical hurdle that is beyond the scope of this study. We expect that the thinning of the fire-affected soil layer could decrease runoff potential and that reductions in sediment availability could lower the likelihood of debris flows, thereby accelerating the crossover (Figure 1a) between postwildfire runoff- and infiltration-generated debris flow probability. Sediment availability in the upper reaches of steep catchments can also change with time, particularly in regions susceptible to postfire raveling (e.g., Tang et al., 2019a; DiBiase & Lamb, 2020). We currently lack observations of the characteristic grain size of the sediment in channels over the multi-annual postwildfire recovery timeline. If the D_{50} coarsens, however, Equation 13 shows that the discharge needed to generate runoff-generated debris would need to increase, thereby reducing the hazard potential. Better quantitative constraints on channel morphology, sediment storage, and particle size distributions could help distinguish debris flows and floods (e.g., Brenna et al., 2020).

6. Summary and Conclusions

Change in debris flow likelihood following wildfire is poorly understood. As an important first step to address this knowledge gap, we develop a method to quantify changes in failure criteria for runoff- and infiltration-generated debris flows throughout the postwildfire soil-hydraulic recovery timeline. At the core of this methodology are physics-based simulations of variably saturated flow that utilize widely available satellite-based postwildfire observations of vegetative reflectance to approximate the time-variable effects of fire on infiltration. When we apply our framework to postwildfire settings in the San Gabriel Mountains of southern California, we find that our results are consistent with in situ soil moisture monitoring, debris flow observations, and existing empirical thresholds for debris flows. The postwildfire soil-hydraulic recovery characteristics that we simulate clearly alter the triggering criteria for runoff- and infiltration-generated debris flows in the years after fire. Our approach also suggests that the probability of debris flow generation processes could be influenced by variability in the rainfall climatology, soil moisture, median grain size, and root reinforcement. As wildfire activity extends into mountainous terrain and climate zones with fewer historical observations of debris flows, our work suggests that a simulation-based framework that can explicitly account for the time-variable effects of fire on soil-hydraulic recovery may be useful to develop warning criteria and improve situational awareness for debris flow hazard in the years following fire.

Data Availability Statement

The in situ soil moisture data that we use to support our analyses are available in Thomas et al. (2021) at <https://doi.org/10.5066/P9QLP6XG>.

Acknowledgments

The authors appreciate the constructive reviews provided by Andrew Gray, Scott McCoy, Paul Santi, Jonathan Perkins, and Donald Lindsay, as well as the thoughtful comments from Joel Sankey, Jeffrey Coe, Brian Shiro, and Janet Slate. Joel Smith and Benjamin Mirus contributed to the siting, installation, and maintenance of the Arroyo Seco and Dunsmore monitoring sites. Luke McGuire was supported in part by the National Oceanic and Atmospheric Administration (NOAA) National Integrated Drought Information System (NIDIS) through Task Order 1332KP-20FNRMT0012. Any use of trade, firm, or product names is for descriptive purposes only and does not imply endorsement by the U.S. Government.

References

- ASTM International (2018). *Standard test method for torsional ring shear test to measure drained fully softened shear strength and stress dependent strength envelope of fine-grained soils*, ASTM International. <https://doi.org/10.1520/D7608-18>
- Baum, R. L., & Godt, J. W. (2010). Early warning of rainfall-induced shallow landslides and debris flows in the USA. *Landslides*, 7(3), 259–272. <https://doi.org/10.1007/s10346-009-0177-0>
- Bell, F. G., & Maud, R. R. (2000). Landslides associated with the colluvial soils overlying the Natal Group in the greater Durban region of Natal, South Africa. *Environmental Geology*, 39(9), 1029–1038. <https://doi.org/10.1007/s002549900077>
- Brenna, A., Surian, N., Ghinassi, M., & Marchi, L. (2020). Sediment-water flows in mountain streams: Recognition and classification based on field evidence. *Geomorphology*, 371, 107413–107418. <https://doi.org/10.1016/j.geomorph.2020.107413>
- Brummer, C. J., & Montgomery, D. R. (2003). Downstream coarsening in headwater channels. *Water Resources Research*, 39(10), 1–14. <https://doi.org/10.1029/2003WR001981>
- Caine, N. (1980). The rainfall intensity - Duration control of shallow landslides and debris flows. *Geografiska Annaler: Series A, Physical Geography*, 62(1/2), 23–27. <https://doi.org/10.2307/52044910.1080/04353676.1980.11879996>
- Campbell, R. H. (1974). Debris flows originating from soil slips during rainstorms in southern California. *Quarterly Journal of Engineering Geology and Hydrogeology*, 7(4), 339–349. <https://doi.org/10.1144/GSL.QJEG.1974.007.04.04>
- Campbell, R. H. (1975). *Soil slips, debris flows, and rainstorms in the Santa Monica Mountains and vicinity, southern California*. Geological Survey Professional Paper 851, 51. <https://doi.org/10.3133/pp851>
- Canfield, H. E., Goodrich, D. C., & Burns, I. S. (2005). Selection of parameter values to model post-fire runoff and sediment transport at the watershed scale in southwestern forests. *ASCE Watershed Management Conference*, 19–22. [https://doi.org/10.1061/40763\(178\)48](https://doi.org/10.1061/40763(178)48)
- Cannon, S. H. (2001). Debris-flow generation from recently burned watersheds. *Environmental and Engineering Geoscience*, 7(4), 321–341. <https://doi.org/10.2113/gsegeosci.7.4.321>
- Cannon, S. H., Gartner, J. E., Wilson, R. C., Bowers, J. C., & Laber, J. L. (2008). Storm rainfall conditions for floods and debris flows from recently burned areas in southwestern Colorado and southern California. *Geomorphology*, 96(3–4), 250–269. <https://doi.org/10.1016/j.geomorph.2007.03.019>
- Casadei, M., Dietrich, W. E., & Miller, N. L. (2003). Testing a model for predicting the timing and location of shallow landslide initiation in soil-mantled landscapes. *Earth Surface Processes and Landforms*, 28(9), 925–950. <https://doi.org/10.1002/esp.470>
- Cerdà, A. (1998). Changes in overland flow and infiltration after a rangeland fire in a Mediterranean scrubland. *Hydrological Processes*, 12(7), 1031–1042. [https://doi.org/10.1002/\(SICI\)1099-1085\(19980615\)12:7<1031::AID-HYP636>3.0.CO;2-V](https://doi.org/10.1002/(SICI)1099-1085(19980615)12:7<1031::AID-HYP636>3.0.CO;2-V)
- CGS. (2020). *Watershed emergency response team evaluation, CZU Lightning Complex*, CGS CA-CZU-005205, 207.
- DeBano, L. F. (2000). The role of fire and soil heating on water repellency in wildland environments: A review. *Journal of Hydrology*, 231–232, 195–206. [https://doi.org/10.1016/S0022-1694\(00\)00194-3](https://doi.org/10.1016/S0022-1694(00)00194-3)
- DeBano, L. F., Rice, R. M., & Conrad, C. E. (1979). Soil heating in chaparral fires: Effects on soil properties, plant nutrients, erosion, and runoff. *U.S. Department of Agriculture Research Paper PSW-145*, 21p. https://www.fs.fed.us/psw/publications/documents/psw_rp145/
- DeGraff, J. V. (2018). A rationale for effective post-fire debris flow mitigation within forested terrain. *Geoenvironmental Disasters*, 5(7), 1–9. <https://doi.org/10.1186/s40677-018-0099-z>
- Delgado, N. (2020). Variation in post-wildfire perturbations to soil hydraulic properties across a climatic gradient. *American Geophysical Union*. Fall Meeting 2020, Abstract #H087-0024.
- DiBiase, R. A., & Lamb, M. P. (2020). Dry sediment loading of headwater channels fuels post-wildfire debris flows in bedrock landscapes. *Geology*, 48(2), 189–193. <https://doi.org/10.1130/G46847.1>
- DiBiase, R. A., Whipple, K. X., Heimsath, A. M., & Ouimet, W. B. (2010). Landscape form and millennial erosion rates in the San Gabriel Mountains, CA. *Earth and Planetary Science Letters*, 289(1–2), 134–144. <https://doi.org/10.1016/j.epsl.2009.10.036>
- Eaton, E. C. (1935). Flood and erosion control problems and their solution. *Proceedings of the American Society of Civil Engineers*, 61(7), 1021–1050. <https://doi.org/10.1061/TACEAT.0004726>
- Ebel, B. A. (2019). Measurement method has a larger impact than spatial scale for plot-scale field-saturated hydraulic conductivity (K_{fs}) after wildfire and prescribed fire in forests. *Earth Surface Processes and Landforms*, 44(10), 1945–1956. <https://doi.org/10.1002/esp.4621>
- Ebel, B. A. (2020). Temporal evolution of measured and simulated infiltration following wildfire in the Colorado front range, USA: Shifting thresholds of runoff generation and hydrologic hazards. *Journal of Hydrology*, 585, 124765. <https://doi.org/10.1016/j.jhydrol.2020.124765>
- Ebel, B. A., Godt, J. W., Lu, N., Coe, J. A., Smith, J. B., & Baum, R. L. (2018). Field and laboratory hydraulic characterization of landslide-prone soils in the Oregon Coast range and implications for hydrologic simulation. *Vadose Zone Journal*, 17(1), 180078–180115. <https://doi.org/10.2136/vzj2018.04.0078>
- Ebel, B. A., & Martin, D. A. (2017). Meta-analysis of field-saturated hydraulic conductivity recovery following wildland fire: Applications for hydrologic model parameterization and resilience assessment. *Hydrological Processes*, 31(21), 3682–3696. <https://doi.org/10.1002/hyp.11288>
- Ebel, B. A., & Moody, J. A. (2020). Parameter estimation for multiple post-wildfire hydrologic models. *Hydrological Processes*, 34(15), 4049–4066. <https://doi.org/10.1002/hyp.13865>
- Ebel, B. A., Rengers, F. K., & Tucker, G. E. (2016). Observed and simulated hydrologic response for a first-order catchment during extreme rainfall 3 years after wildfire disturbance. *Water Resources Research*, 52(12), 9367–9389. <https://doi.org/10.1002/2016WR019110>
- Ferguson, R. (2007). Flow resistance equations for gravel- and boulder-bed streams. *Water Resources Research*, 43(5), 1–12. <https://doi.org/10.1029/2006WR005422>
- Freeze, R. A., & Cherry, J. A. (1979). *Groundwater* (pp. 604). Englewood Cliffs, NJ: Prentice Hall.
- Gabet, E. J., & Bookter, A. (2008). A morphometric analysis of gullies scoured by post-fire progressively bulked debris flows in southwest Montana, USA. *Geomorphology*, 96(3–4), 298–309. <https://doi.org/10.1016/j.geomorph.2007.03.016>
- Gehring, E., Conedera, M., Maringer, J., Giadrossich, F., Guastini, E., & Schwarz, M. (2019). Shallow landslide disposition in burnt European beech (*Fagus sylvatica* L.) forests. *Scientific Reports*, 9(1), 2045–2322. <https://doi.org/10.1038/s41598-019-45073-7>

- Godt, J. W., & McKenna, J. P. (2008). Numerical modeling of rainfall thresholds for shallow landsliding in the Seattle, Washington area. In R. L. Baum, J. W. Godt, & L. M. Highland (Eds.), *Engineering geology and landslides of the Seattle, Washington area* (pp. 121–135). Boulder, CO: Geological Society of America. [https://doi.org/10.1130/2008.4020\(07\)](https://doi.org/10.1130/2008.4020(07))
- Grayson, R. B., Western, A. W., Chiew, F. H. S., & Blöschl, G. (1997). Preferred states in spatial soil moisture patterns: Local and nonlocal controls. *Water Resources Research*, *33*(12), 2897–2908. <https://doi.org/10.1029/97WR02174>
- Gregoretti, C., & Fontana, G. D. (2008). The triggering of debris flow due to channel-bed failure in some alpine headwater basins of the Dolomites: Analyses of critical runoff. *Hydrological Processes*, *22*(13), 2248–2263. <https://doi.org/10.1002/hyp.6821>
- Güllinger, J. J., Gray, A. B., Barth, N. C., & Fong, B. T. (2020). The evolution of sediment sources over a sequence of postfire sediment-laden flows revealed through repeat high-resolution change detection. *Journal of Geophysical Research*, *125*(10), 1–23. <https://doi.org/10.1029/2020JF005527>
- Guzzetti, F., Peruccacci, S., Rossi, M., & Stark, C. P. (2007). Rainfall thresholds for the initiation of landslides in central and southern Europe. *Meteorology and Atmospheric Physics*, *98*, 239–267. <https://doi.org/10.1007/s00703-007-0262-7>
- Halsey, R. W. (2005). *Fire, chaparral, and survival in southern California* (p. 232). El Cajon, CA: Sunbelt Publications, Inc.
- Hargreaves, G. H. (1994). Defining and using reference evapotranspiration. *Journal of Irrigation and Drainage Engineering*, *120*(6), 1132–1139. [https://doi.org/10.1061/\(ASCE\)0733-9437\(1994\)120:6\(1132\)](https://doi.org/10.1061/(ASCE)0733-9437(1994)120:6(1132))
- Hong, Y., Hiura, H., Shino, K., Sassa, K., Suemine, A., Fukuoka, H., & Wang, G. (2005). The influence of intense rainfall on the activity of large-scale crystalline schist landslides in Shikoku Island, Japan. *Landslides*, *2*, 97–105. <https://doi.org/10.1007/s10346-004-0043-z>
- Hubbert, K. R., & Oriol, V. (2005). Temporal fluctuations in soil water repellency following wildfire in chaparral steeplands, southern California. *International Journal of Wildland Fire*, *14*(4), 439–447. <https://doi.org/10.1071/WF05036>
- Iverson, R. M. (2000). Landslide triggering by rain infiltration. *Water Resources Research*, *36*(7), 1897–1910. <https://doi.org/10.1029/2000WR900090>
- Jackson, M., & Roering, J. J. (2009). Post-fire geomorphic response in steep, forested landscapes: Oregon Coast Range, USA. *Quaternary Science Reviews*, *28*(11–12), 1131–1146. <https://doi.org/10.1016/j.quascirev.2008.05.003>
- Jennings, C. W., Strand, R. G., & Rogers, T. H. (1977). *Geologic map of California (geologic data map 2)*, Sacramento, California: Division of Mines and Geology, scale, 1:750,000.
- Katsura, S., Kosugi, K., Mizutani, T., & Mizuyama, T. (2009). Hydraulic properties of variously weathered granitic bedrock in headwater catchments. *Vadose Zone Journal*, *8*(3), 557–573. <https://doi.org/10.2136/vzj2008.0142>
- Kean, J. W., McGuire, L. A., Rengers, F. K., Smith, J. B., & Staley, D. M. (2016). Amplification of postwildfire peak flow by debris. *Geophysical Research Letters*, *43*(16), 8545–8553. <https://doi.org/10.1002/2016GL069661>
- Kean, J. W., Smith, J. B., Rengers, F. K., McGuire, L. A., & Staley, D. M. (2019). Post-wildfire debris-flow monitoring data, Las Lomas, 2016 Fish Fire, Los Angeles county, California, November 2016 to February 2017. *U.S. Geological Survey data release*. <https://doi.org/10.5066/P9F3YTBP>
- Kean, J. W., & Staley, D. M. (2021). Forecasting the frequency and magnitude of postfire debris flows across southern California. *Earth's Future*, *9*, e2020EF001735. <https://doi.org/10.1029/2020EF001735>
- Kean, J. W., Staley, D. M., & Cannon, S. H. (2011). In situ measurements of post-fire debris flows in southern California: Comparisons of the timing and magnitude of 24 debris-flow events with rainfall and soil moisture conditions. *Journal of Geophysical Research*, *116*(F4), 1–21. <https://doi.org/10.1029/2011JF002005>
- Kean, J. W., Staley, D. M., Lancaster, J. T., Rengers, F. K., Swanson, B. J., Coe, J. A., et al. (2019). Inundation, flow dynamics, and damage in the 9 January 2018 Montecito debris-flow event, California, USA: Opportunities and challenges for post-wildfire risk assessment. *Geosphere*, *15*(4), 1140–1163. <https://doi.org/10.1130/GES02048.1>
- Kotok, E. I., & Kraebel, C. J. (1935). Discussion of “Flood and erosion control problems and their solution”. *ASCE Transactions*, *101*, 1350–1355.
- Langhans, C., Lane, P. N. J., Nyman, P., Noske, P. J., Cawson, J. G., Oono, A., & Sheridan, G. J. (2016). Scale-dependency of effective hydraulic conductivity on fire-affected hillslopes. *Water Resources Research*, *52*(7), 5041–5055. <https://doi.org/10.1002/2016WR018998>
- Larsen, I. J., MacDonald, L. H., Brown, E., Rough, D., Welsh, M. J., Pietraszek, J. H., et al. (2009). Causes of post-fire runoff and erosion: Water repellency, cover, or soil sealing? *Soil Science Society of America Journal*, *73*(4), 1393–1407. <https://doi.org/10.2136/sssaj2007.0432>
- Larsen, M. C., & Simon, A. (1993). A rainfall intensity-duration threshold for landslides in a humid-tropical environment, Puerto Rico. *Geografiska Annaler - Series A: Physical Geography*, *75*(1/2), 13–23. <https://doi.org/10.1080/04353676.1993.1188037910.2307/521049>
- Lavé, J., & Burbank, D. (2004). Denudation processes and rates in the Transverse Ranges, southern California: Erosional response of a transitional landscape to external and anthropogenic forcing. *Journal of Geophysical Research*, *109*(F1), 148–227. <https://doi.org/10.1029/2003JF000023>
- Lu, N., & Godt, J. (2008). Infinite slope stability under steady unsaturated seepage conditions. *Water Resources Research*, *44*(11), 1–13. <https://doi.org/10.1029/2008WR006976>
- Lu, N., & Godt, J. (2013). *Hillslope hydrology and stability*. Cambridge, UK: University Press. 437 p. <https://doi.org/10.1017/CBO9781139108164>
- McGuire, L. A., Rengers, F. K., Kean, J. W., Coe, J. A., Mirus, B. B., Baum, R. L., & Godt, J. W. (2016). Elucidating the role of vegetation in the initiation of rainfall-induced shallow landslides: Insights from an extreme rainfall event in the Colorado front range. *Geophysical Research Letters*, *43*(17), 9084–9092. <https://doi.org/10.1002/2016GL070741>
- McGuire, L. A., Rengers, F. K., Kean, J. W., Staley, D. M., & Mirus, B. B. (2018). Incorporating spatially heterogeneous infiltration capacity into hydrologic models with applications for simulating post-wildfire debris flow initiation. *Hydrological Processes*, *32*(9), 1173–1187. <https://doi.org/10.1002/hyp.11458>
- McGuire, L. A., Rengers, F. K., Oakley, N., Kean, J. W., Staley, D. M., Tang, H., et al. (2021). Time since burning and rainfall characteristics impact post-fire debris-flow initiation and magnitude. *Environmental and Engineering Geoscience*, *27*(1), 43–56. <https://doi.org/10.2113/EEG-D-20-00029>
- McGuire, L. A., Rengers, F. K., & Tang, H. (2019). *Evolving thresholds for mass-movement following disturbance by fire*. American Geophysical Union, Fall Meeting 2019, Abstract #EP31B-01. <https://doi.org/10.1287/18ae9c30-669a-4cb2-8896-213ccba7a67a>
- McGuire, L. A., & Youberg, A. M. (2020). What drives spatial variability in rainfall intensity-duration thresholds for post-wildfire debris flows? Insights from the 2018 Buzzard Fire, NM, USA. *Landslides*, *17*, 2385–2399. <https://doi.org/10.1007/s10346-020-01470-y>
- McPhee, J. A. (1989). *The control of nature* (pp. 272). New York, NY: Farrar, Straus, and Giroux.
- Meng, R., Dennison, P. E., D'Antonio, C. M., & Moritz, M. A. (2014). Remote sensing analysis of vegetation recovery following short-interval fires in southern California shrublands. *PloS One*, *9*(10), e110637. <https://doi.org/10.1371/journal.pone.0110637>
- Meter Group. (2020). *EC-5 (Operator's Manual)* (pp. 21). Pullman, WA: Meter Group.

- Meyer, G. A., Pierce, J. L., Wood, S. H., & Jull, A. J. T. (2001). Fire, storms, and erosional events in the Idaho batholith. *Hydrological Processes*, 15(15), 3025–3038. <https://doi.org/10.1002/hyp.389>
- Mirus, B. B., Staley, D. M., Kean, J. W., Smith, J. B., Wooten, R., McGuire, L. A., & Ebel, B. A. (2019). Towards a conceptual framework for assessing disturbance impacts on debris-flow initiation thresholds across hydroclimatic settings. In J. W. Kean, J. A. Coe, O. M. Santi, & B. K. Guillen (Eds.), *Proceedings of the 7th international conference on debris-flow hazards mitigation* (pp. 524–531). <https://doi.org/10.25676/11124/173176>
- Moody, J. A., & Ebel, B. A. (2014). Infiltration and runoff generation processes in fire-affected soils. *Hydrological Processes*, 28(9), 3432–3453. <https://doi.org/10.1002/hyp.9857>
- Moody, J. A., Shakesby, R. A., Robichaud, P. R., Cannon, S. H., & Martin, D. A. (2013). Current research issues related to post-wildfire runoff and erosion processes. *Earth-Science Reviews*, 122, 10–37. <https://doi.org/10.1016/j.earscirev.2013.03.004>
- Mualem, Y. (1976). A new model for predicting the hydraulic conductivity of unsaturated porous media. *Water Resources Research*, 12(3), 513–522. <https://doi.org/10.1029/WR012i003p00513>
- NASA. (2020). MOD15A2H v006, “MODIS/Terra+Aqua Leaf Area Index/FPAR 8-Day L4 Global 500 m SIN Grid”. available from: <https://lpdaac.usgs.gov/products/mcd15a2hv006/> (accessed 22 December 2020).
- NOAA. (2020). “NOAA ATLAS 14 point precipitation frequency estimates.”. *Hydrometeorological design studies center*. available from: https://hdsc.nws.noaa.gov/hdsc/pfds/pfds_map_cont.html (accessed 22 December 2020).
- Novak, D. R., Bailey, C., Brill, K. F., Burke, P., Hogsett, W. A., Rausch, R., & Schichtel, M. (2014). Precipitation and temperature forecast performance at the weather prediction center. *Weather and Forecasting*, 29, 489–504. <https://doi.org/10.1175/WAF-D-13-00066.1>
- Nyman, P., Sheridan, G. J., Moody, J. A., Smith, H. G., Noske, P. J., & Lane, P. N. J. (2013). Sediment availability on burned hillslopes. *Journal of Geophysical Research: Earth Surface*, 118(4), 2451–2467. <https://doi.org/10.1002/jgrf.20152>
- Nyman, P., Sheridan, G. J., Smith, H. G., & Lane, P. N. J. (2011). Evidence of debris flow occurrence after wildfire in upland catchments of south-east Australia. *Geomorphology*, 125(3), 383–401. <https://doi.org/10.1016/j.geomorph.2010.10.016>
- Nyman, P., Sheridan, G. J., Smith, H. G., & Lane, P. N. J. (2014). Modeling the effects of surface storage, macropore flow and water repellency on infiltration after wildfire. *Journal of Hydrology*, 513, 301–313. <https://doi.org/10.1016/j.jhydrol.2014.02.044>
- Palucis, M. C., Ulizio, T. P., & Lamb, M. P. (2021). Debris flow initiation from ravel-filled channel bed failure following wildfire in a bedrock landscape with limited sediment supply. *Geological Society of America Bulletin*. <https://doi.org/10.1130/B35822.1>
- Parise, M., & Cannon, S. H. (2012). Wildfire impacts on the processes that generate debris flows in burned watersheds. *Natural Hazards*, 61(1), 217–227. <https://doi.org/10.1007/s11069-011-9769-9>
- Parks, D. S., & Cundy, T. W. (1989). *Soil hydraulic characteristics of a small southwest Oregon watershed following high-intensity wildfires*. U.S. Department of Agriculture General Technical Report PSW-109, pp. 5. <https://doi.org/10.3133/ofr97745F>
- PRISM Climate Group. (2020). *30-Year Normals*. “30-yr Normal Precipitation: Annual,” available from: <http://www.prism.oregonstate.edu/normals/> accessed 22 December 2020.
- Raymond, C. A., McGuire, L. A., Youberg, A. M., Staley, D. M., & Kean, J. W. (2020). Thresholds for post-wildfire debris flows: Insights from the Pinal Fire, Arizona, USA. *Earth Surface Processes and Landforms*, 45(6), 1349–1360. <https://doi.org/10.1002/esp.4805>
- Regelbrugge, J., & Conard, S. (1993). Modeling tree mortality following wildfire in Pinus ponderosa forests in the central Sierra-Nevada of California. *International Journal of Wildland Fire*, 3(3), 139–148. <https://doi.org/10.1071/WF9930139>
- Rengers, F. K. (2020). *Inventory of landslides triggered by rainfall on 16-17 January 2019, Los Angeles County, CA*. U.S. Geological Survey data release. <https://doi.org/10.5066/P97GU3UV>
- Rengers, F. K., McGuire, L. A., Kean, J. W., Staley, D. M., & Hobbey, D. E. J. (2016). Model simulations of flood and debris flow timing in steep catchments after wildfire. *Water Resources Research*, 52(8), 6041–6061. <https://doi.org/10.1002/2015WR018176>
- Rengers, F. K., McGuire, L. A., Kean, J. W., Staley, D. M., & Youberg, A. M. (2019). Progress in simplifying hydrologic model parameterization for broad applications to post-wildfire flooding and debris-flow hazards. *Earth Surface Processes and Landforms*, 44(15), 3078–3092. <https://doi.org/10.1002/esp.4697>
- Rengers, F. K., McGuire, L. A., Oakley, N. S., Kean, J. W., Staley, D. M., & Tang, H. (2020). Landslides after wildfire: Initiation, magnitude, and mobility. *Landslides*, 17(11), 2631–2641. <https://doi.org/10.1007/s10346-020-01506-3>
- Rengers, F. K., Pagonis, V., & Mahan, S. A. (2017). Can thermoluminescence be used to determine soil heating from a wildfire? *Radiation Measurements*, 107, 119–127. <https://doi.org/10.1016/j.radmeas.2017.09.002>
- Rengers, F. K., Tucker, G. E., Moody, J. A., & Ebel, B. A. (2016). Illuminating wildfire erosion and deposition patterns with repeat terrestrial lidar. *Journal of Geophysical Research: Earth Surface*, 121(3), 588–608. <https://doi.org/10.1002/2015JF003600>
- Rice, R. M., & Foggin, G. T. (1971). Effect high intensity storms on soil slippage on mountainous watersheds in Southern California. *Water Resources Research*, 7(6), 1485–1496. <https://doi.org/10.1029/WR007i006p01485>
- Richards, L. A. (1931). Capillary conduction of liquids through porous mediums. *Physics*, 1(5), 318–333. <https://doi.org/10.1063/1.1745010>
- Sankey, J. B., Kreitler, J., Hawbaker, T. J., McVay, J. L., Miller, M. E., Mueller, E. R., et al. (2017). Climate, wildfire, and erosion ensemble foretells more sediment in western USA watersheds. *Geophysical Research Letters*, 44(17), 8884–8892. <https://doi.org/10.1002/2017GL073979>
- Santi, P. M., & MacAulay, B. (2021). Water and sediment supply requirements for post-wildfire debris flows in the western United States. *Environmental and Engineering Geoscience*, 27(1), 73–85. <https://doi.org/10.2113/EEG-D-20-00022>
- Santi, P. M., & Rengers, F. K. (2020). Wildfire and landscape change. *Reference Module in Earth Systems and Environmental Sciences*. United States Geological Survey, <https://doi.org/10.1016/B978-0-12-818234-5.00017-1>
- Schaap, M. G. (1999). *Rosetta Version 1.0 Documentation*. (p. 4). U.S. Department of Agriculture.
- Schmidt, K. M., Roering, J. J., Stock, J. D., Dietrich, W. E., Montgomery, D. R., & Schaub, T. (2001). The variability of root cohesion as an influence on shallow landslide susceptibility in the Oregon Coast Range. *Canadian Geotechnical Journal*, 38(1), 995–1024. <https://doi.org/10.1139/t01-031>
- Shakeby, R. A., & Doerr, S. H. (2006). Wildfire as a hydrological and geomorphological agent. *Earth-Science Reviews*, 74(3–4), 269–307. <https://doi.org/10.1016/j.earscirev.2005.10.006>
- Shakesby, R. A., Coelho, C., Ferreira, A., Terry, J., & Walsh, R. (1993). Wildfire impacts on soil-erosion and hydrology in wet Mediterranean forest, Portugal. *International Journal of Wildland Fire*, 3(2), 95–110. <https://doi.org/10.1071/WF9930095>
- Sheridan, G. J., Lane, P. N. J., & Noske, P. J. (2007). Quantification of hillslope runoff and erosion processes before and after wildfire in a wet Eucalyptus forest. *Journal of Hydrology*, 343(1–2), 12–28. <https://doi.org/10.1016/j.jhydrol.2007.06.005>
- Šimůnek, J., Šejna, M., Saito, H., Sakai, M., van Genuchten, & MTh (2009). *The Hydrus-1D software package for simulating the one-dimensional movement of water, heat, and multiple solutes in variably-saturated media* (pp. 332). University of California Riverside, Version 4.08 Documentation.

- Skaggs, T. H., van Genuchten, M. T., Shouse, P. J., & Poss, J. A. (2006). Macroscopic approaches to root water uptake as a function of water and salinity stress. *Agricultural Water Management*, 86(1–2), 140–149. <https://doi.org/10.1016/j.agwat.2006.06.005>
- Smith, J. B., Kean, J. W., Mirus, B. B., Staley, D. M., Rengers, F. K., & McGuire, L. A. (2019). *Hillslope hydrologic monitoring data following the 2009 Station Fire, Los Angeles County, California, November 2015 to June 2017*. U.S. Geological Survey data release. <https://doi.org/10.5066/P98G0FS2>
- Smith, R. E., & Goodrich, D. C. (2000). Model for rainfall excess patterns on randomly heterogeneous areas. *Journal of Hydrologic Engineering*, 5(4), 355–362. [https://doi.org/10.1061/\(ASCE\)1084-0699\(2000\)5:4\(355\)](https://doi.org/10.1061/(ASCE)1084-0699(2000)5:4(355))
- Staley, D. M., Kean, J. W., Cannon, S. H., Schmidt, K. M., & Laber, J. L. (2013). Objective definition of rainfall intensity-duration thresholds for the initiation of post-fire debris flows in southern California. *Landslides*, 10(5), 547–562. <https://doi.org/10.1007/s10346-012-0341-9>
- Staley, D. M., Kean, J. W., & Rengers, F. K. (2020). The recurrence interval of post-fire debris-flow generating rainfall in the southwestern United States. *Geomorphology*, 370, 107392–107410. <https://doi.org/10.1016/j.geomorph.2020.107392>
- Staley, D. M., Negri, J. A., Kean, J. W., Laber, J. L., Tillery, A. C., & Youberg, A. M. (2017). Prediction of spatially explicit rainfall intensity-duration thresholds for post-fire debris-flow generation in the western United States. *Geomorphology*, 278, 149–162. <https://doi.org/10.1016/j.geomorph.2016.10.019>
- Staley, D. M., Wasklewicz, T. A., & Kean, J. W. (2014). Characterizing the primary material sources and dominant erosional processes for post-fire debris-flow initiation in a headwater basin using multi-temporal terrestrial laser scanning data. *Geomorphology*, 214, 324–338. <https://doi.org/10.1016/j.geomorph.2014.02.015>
- Tang, H., McGuire, L. A., Rengers, F. K., Kean, J. W., Staley, D. M., & Smith, J. B. (2019). Evolution of debris-flow initiation mechanisms and sediment sources during a sequence of postwildfire rainstorms. *Journal of Geophysical Research: Earth Surface*, 124(6), 1572–1595. <https://doi.org/10.1029/2018JF004837>
- Terwilliger, V. J., & Waldron, L. J. (1990). Assessing the contribution of roots to the strength of undisturbed, slip prone soils. *Catena*, 17(12), 151–162. [https://doi.org/10.1016/0341-8162\(90\)90005-X](https://doi.org/10.1016/0341-8162(90)90005-X)
- Terwilliger, V. J., & Waldron, L. J. (1991). Effects of root reinforcement on soil-slip patterns in the transverse ranges of southern California. *Geological Society of America Bulletin*, 103(6), 775–785. [https://doi.org/10.1130/0016-7606\(1991\)103<0775:EOOROS>2.3.CO;2](https://doi.org/10.1130/0016-7606(1991)103<0775:EOOROS>2.3.CO;2)
- Thomas, M. A., Kean, J. W., Smith, J. B., Mirus, B. B., Staley, D. M., Rengers, F. K., & McGuire, L. A. (2021). Soil moisture monitoring following the 2009 Station Fire, California, USA, 2016–2019. U.S. Geological Survey data release. <https://doi.org/10.5066/P9QLP6XG>
- Thomas, M. A., Mirus, B. B., & Collins, B. D. (2018). Identifying physics-based thresholds for rainfall-induced landsliding. *Geophysical Research Letters*, 45(18), 9651–9661. <https://doi.org/10.1029/2018GL079662>
- Thomas, M. A., Mirus, B. B., Collins, B. D., Lu, N., & Godt, J. W. (2018). Variability in soil-water retention properties and implications for physics-based simulation of landslide early warning criteria. *Landslides*, 15, 1265–1277. <https://doi.org/10.1007/s10346-018-0950-z>
- USDA. (2020). *Web Soil Survey, "Soil Data Explorer"*. available from: <https://websoilsurvey.sc.egov.usda.gov/App/HomePage.htm> accessed 22 December 2020.
- USDA. (2021). *BAER Home, "BAER Imagery Support Data Download"*. available from: <https://fsapps.nwgc.gov/baer/> accessed 29 March 2021.
- USGS. (2005). *NOAA-USGS debris-flow warning system - final report*. US Geological Survey Circular 1283, 60. <https://doi.org/10.3133/cir1283>
- USGS. (2020). *Online spatial data, "California geologic map data"*. available from: <https://mrddata.usgs.gov/geology/state/state.php?state=CA> accessed 22 December 2020.
- van Genuchten, M. T. (1980). A closed-form equation for predicting the hydraulic conductivity of unsaturated soils. *Soil Science Society of America Journal*, 44(5), 892–898. <https://doi.org/10.2136/sssaj1980.03615995004400050002x>
- Varnes, D. J. (1978). Slope movement types and processes. In R. L. Schuster, & R. J. Krizek (Eds.), *Landslides, analysis and control, special report* (pp. 11–33). Washington, DC: Transportation Research Board, National Academy of Sciences.
- von Hoyningen-Hüene, J. (1983). Die interzeption des niederschlags in landwirtschaftlichen pflanzenbeständen. *Schriftenreihe des Deutschen Verbandes fuer Wasserwirtschaft und Kulturbau*, 57, 1–53.
- Watson, D. J. (1947). Comparative physiological studies on the growth of field crops: I. Variation in net assimilation rate and leaf area between species and varieties, and within and between years. *Annals of Botany*, 11(44), 41–76. <https://doi.org/10.1093/oxfordjournals.aob.a08314810.1093/oxfordjournals.aob.a083165>
- Westerling, A. L., Hidalgo, H. G., Cayan, D. R., & Swetnam, T. W. (2006). Warming and earlier spring increase western U.S. forest wildfire activity. *Science*, 313(5789), 940–943. <https://doi.org/10.1126/science.1128834>
- Wieczorek, G. F., Harp, E. L., & Mark, R. K. (1988). Debris flows and other landslides in San Mateo, Santa Cruz, Contra Costa, Alameda, Napa, Solano, Sonoma, Lake and Yolo Counties, and factors influencing debris-flow distribution. In: *Landslides, floods, and marine effects of the storm of January 3–5, 1982, in the San Francisco Bay region*. U.S. Geological Survey Professional Paper 1434, pp. 133–161.
- Wilson, R. C., & Jayko, A. S. (1997). Preliminary maps showing rainfall thresholds for debris-flow activity, San Francisco Bay region, California. *Geological Survey Open-File Report*, 97–745F, 20. <https://doi.org/10.3133/ofr97745F>
- Wondzell, S. M., & King, J. G. (2003). Postfire erosional processes in the Pacific Northwest and Rocky Mountain regions. *Forest Ecology and Management*, 178(1–2), 75–87. [https://doi.org/10.1016/S0378-1127\(03\)00054-9](https://doi.org/10.1016/S0378-1127(03)00054-9)